Cell Stem Cell

Article

A DLG1-ARHGAP31-CDC42 axis is essential for the intestinal stem cell response to fluctuating niche Wnt signaling

Graphical abstract

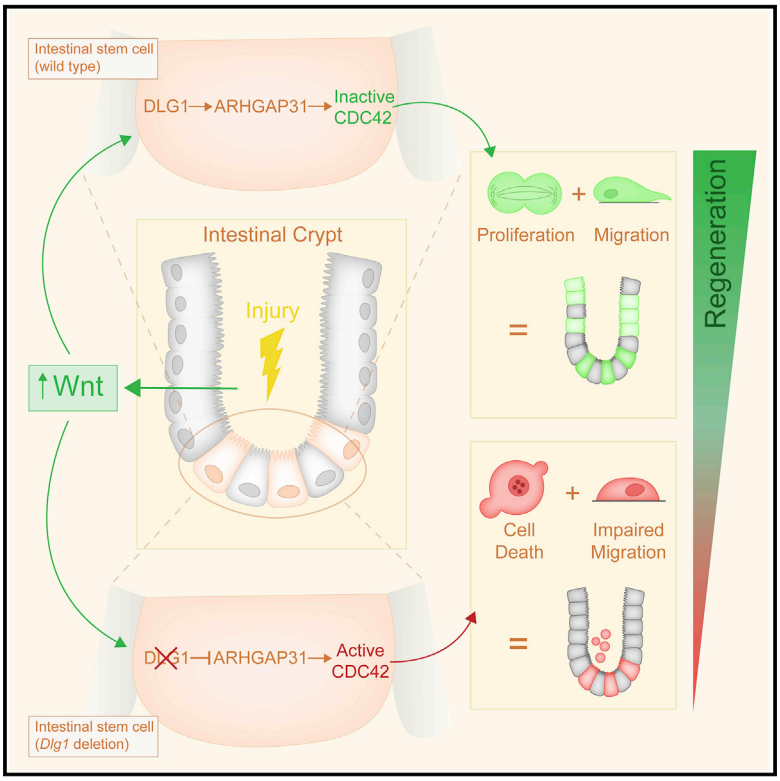

Highlights

- Polarity of the mammalian intestinal epithelium is independent of *Dlg1*
- Loss of *Dlg1* in ISCs results in cell death under high Wnt conditions
- ISCs lacking *Dlg1* have impaired cell division and migration
- Canonical WNT ligands activate non-canonical Wnt signaling via DLG1-ARHGAP31-CDC42

Authors

David Castillo-Azofeifa, Tomas Wald, Efren A. Reyes, ..., Mary K. Estes, Todd Nystul, Ophir D. Klein

Correspondence

ophir.klein@cshs.org

In brief

Throughout an organism's life, the activity of niche signals fluctuates due to injury, and stem cells need to respond accordingly. Klein and colleagues found that during high Wnt activity observed in intestinal regeneration, niche canonical WNT ligands activate non-canonical Wnt signaling via a DLG1-ARHGAP31-CDC42 axis required for stem cell-driven regeneration.

Castillo-Azofeifa et al., 2023, Cell Stem Cell *30*, 188–206
February 2, 2023 © 2022 Elsevier Inc.
https://doi.org/10.1016/j.stem.2022.12.008

CellPress

CellPress

Cell Stem Cell

Article

A DLG1-ARHGAP31-CDC42 axis is essential for the intestinal stem cell response to fluctuating niche Wnt signaling

David Castillo-Azofeifa,[1,2,10] Tomas Wald,[1,10] Efren A. Reyes,[1,3] Aaron Gallagher,[1] Julia Schanin,[1] Stephanie Vlachos,[4] Nathalie Lamarche-Vane,[5,6] Carolyn Bomidi,[7] Sarah Blutt,[7] Mary K. Estes,[7] Todd Nystul,[4] and Ophir D. Klein[1,8,9,11,*]
[1]Department of Orofacial Sciences and Program in Craniofacial Biology, University of California, San Francisco, San Francisco, CA, USA
[2]Department of Regenerative Medicine, Genentech, Inc., South San Francisco, CA, USA
[3]Department of Pharmaceutical Chemistry and TETRAD Program, University of California, San Francisco, San Francisco, CA, USA
[4]Department of Anatomy, University of California, San Francisco, San Francisco, CA, USA
[5]Cancer Research Program, Research Institute of the McGill University Health Centre, Montréal, QC, Canada
[6]Department of Anatomy and Cell Biology, McGill University, Montréal, QC, Canada
[7]Department of Molecular Virology and Microbiology, Baylor College of Medicine, Houston, TX, USA
[8]Department of Pediatrics and Institute for Human Genetics, University of California, San Francisco, San Francisco, CA, USA
[9]Department of Pediatrics, Cedars-Sinai Medical Center, Los Angeles, CA, USA
[10]These authors contributed equally
[11]Lead contact
*Correspondence: ophir.klein@cshs.org
https://doi.org/10.1016/j.stem.2022.12.008

SUMMARY

A central factor in the maintenance of tissue integrity is the response of stem cells to variations in the levels of niche signals. In the gut, intestinal stem cells (ISCs) depend on Wnt ligands for self-renewal and proliferation. Transient increases in Wnt signaling promote regeneration after injury or in inflammatory bowel diseases, whereas constitutive activation of this pathway leads to colorectal cancer. Here, we report that Discs large 1 (*Dlg1*), although dispensable for polarity and cellular turnover during intestinal homeostasis, is required for ISC survival in the context of increased Wnt signaling. RNA sequencing (RNA-seq) and genetic mouse models demonstrated that DLG1 regulates the cellular response to increased canonical Wnt ligands. This occurs via the transcriptional regulation of *Arhgap31*, a GTPase-activating protein that deactivates CDC42, an effector of the non-canonical Wnt pathway. These findings reveal a DLG1-ARHGAP31-CDC42 axis that is essential for the ISC response to increased niche Wnt signaling.

INTRODUCTION

Epithelial tissues have extraordinary resilience against physical and chemical damage, in part due to rapid regeneration fueled by stem cells.[1] Stem cells are essential for maintaining tissue function and ensuring a return to homeostasis after injury.[2] The small intestinal epithelium is a multifunctional tissue that performs essential tasks, including nutrient absorption and maintenance of a barrier against harmful pathogens and carcinogens that are ingested. The epithelial lining is made up of repetitive units of villus-crypt structures. At the base of each villus, tubular crypts house proliferative LGR5$^+$ intestinal stem cells (ISCs)[3] that continuously replenish the entire human and mouse epithelium within 3–5 days. Indeed, the gut lining is the most rapidly cycling epithelium in the mammalian body and thus provides an excellent model to study somatic stem cells.[4,5] ISCs actively proliferate to self-renew and generate transit-amplifying (TA) progenitor cells, which in turn give rise to differentiated absorptive and secretory cells.[3,6]

The regenerative potential of stem cells depends on microenvironmental cues from the stem cell niche.[7] As a result of ever-changing tissue needs, such as growth during development and repair during regeneration, niche signals required for stem cell activity fluctuate throughout life.[8–10] In the intestine, epithelial and mesenchymal Wnt signals are a central part of the molecular milieu responsible for ISC function.[6,11–19] During intestinal homeostasis, Wnt signals regulate ISCs to maintain steady-state conditions.[20–24] After injury, such as by irradiation, inflammation, resection, or infection, the regeneration of the intestinal epithelium is driven by transient increases in expression of Wnt ligands followed by robust pathway activation that promotes proliferation and stemness.[17,25–30] However, the constitutive activation of Wnt signaling can lead to tumorigenesis,[31–35] which in the intestine often occurs through mutation of the tumor suppressor adenomatous polyposis coli (APC).[20–24,36] Even though the Wnt pathway has been extensively studied in the intestinal epithelium, it remains unclear how stem cells contend with the transient increases in Wnt signaling that occur throughout life.

 © 2022 Elsevier Inc.

CellPress

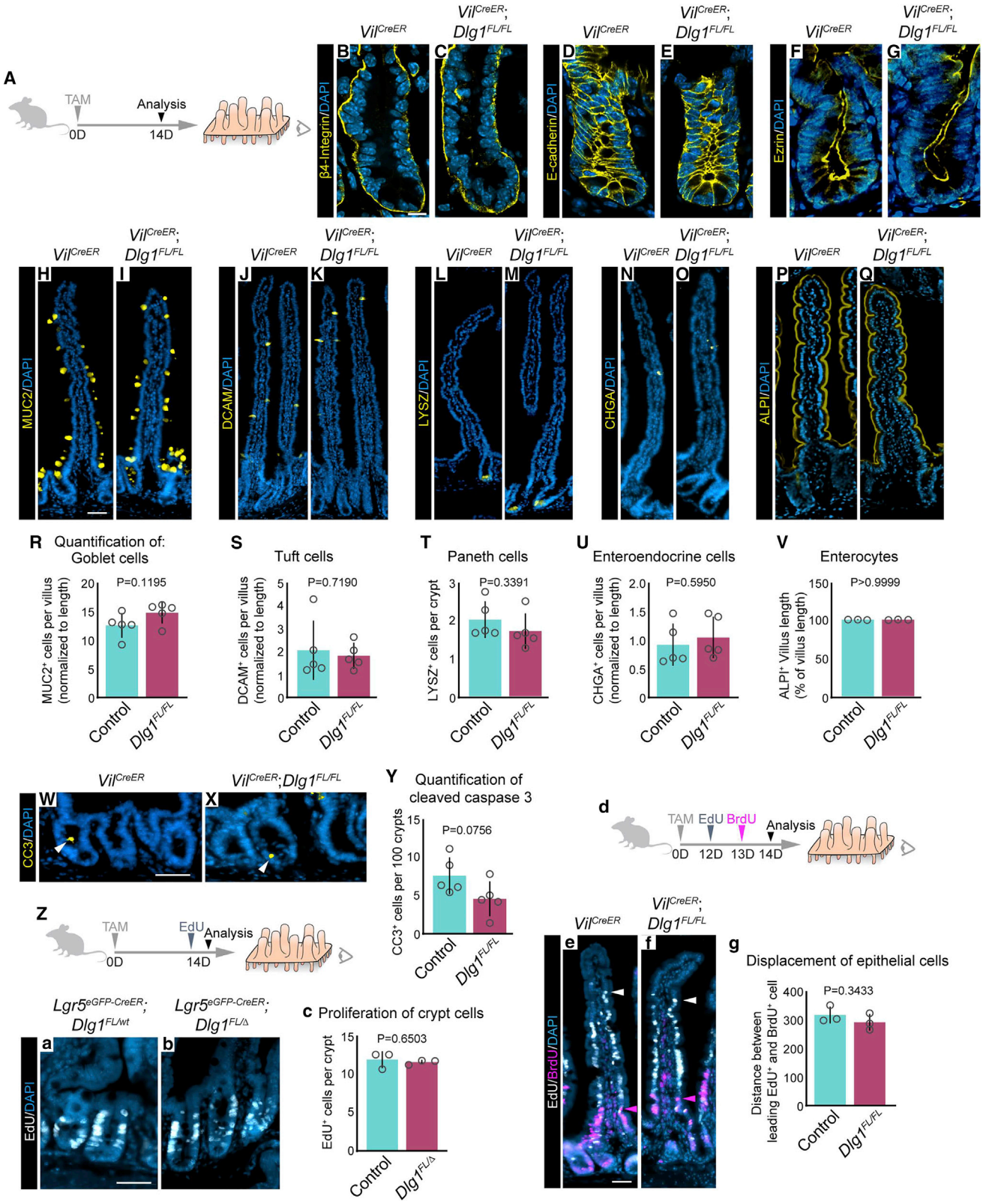

Figure 1. Polarity and integrity of the intestinal epithelium do not depend on the canonical polarity factor DLG1

(A) Mice were injected with one dose of tamoxifen (TAM) and the small intestinal epithelium was analyzed 14 days later.

(B–Q) Immunofluorescence images of mAbs for adhesion molecules and differentiation markers. Scale bars, 10 μm (B–G) and 50 μm (H–Q).

(legend continued on next page)

APC interacts with Discs large 1 (DLG1),[37–39] a tumor suppressor protein that is part of the Scribble polarity complex (together with SCRIBBLE and lethal giant larvae) and is classically known to regulate cell polarity by directing the formation of basolateral membranes.[37,39–41] The deletion of Scribble polarity proteins leads to severe developmental abnormalities in several organs in invertebrates and vertebrates.[42–45] Likewise, the deletion of intestinal *Scribble* has a profound effect on apical-basal polarity in the adult intestine.[46] However, the deletion of *Drosophila* midgut *Dlg* is dispensable for midgut polarity.[47]

Potential intersections between Wnt/β-catenin signaling and DLG1-mediated polarity have been reported using *in vitro* approaches. These studies demonstrated the importance of interactions between APC and DLG1 for various cellular functions: polarization of migrating astrocytes,[48] cell cycle progression in fibroblasts,[49] and the migration of isolated Xenopus epithelial cells.[50] The deletion of *Dlg1* in the intestine decreases the survival of mice harboring tumorigenic *Apc* mutations, demonstrating the involvement of DLG1 in the Wnt signaling pathway.[51] However, the molecular and cellular mechanisms underlying the role of DLG1 in Wnt signaling is not clear.

In this study, we investigated the link between DLG1 and canonical Wnt signaling in the intestinal epithelium by conditionally deleting *Dlg1* using intestinal *Vil*^{CreER} and ISC-specific *Lgr5*^{CreER} drivers. During homeostasis, intestinal cell turnover and apical-basal polarization were not affected by the absence of *Dlg1*, consistent with data from the *Drosophila* midgut.[47] However, we found that *Dlg1* is required for the proper intestinal response to increased canonical Wnt levels. *Dlg1* regulates the expression of *Arhgap31*, a GTPase-activating protein that regulates the activity of the small GTPase CDC42, which in turn is an effector of the non-canonical Wnt planar cell polarity pathway.[52,53] These findings shed light on a previously underappreciated crosstalk between canonical Wnt ligands and the non-canonical Wnt pathway which ISCs rely on during WNT-dependent regeneration.

RESULTS

Dlg1 is dispensable for mammalian intestinal polarity maintenance and epithelial integrity during homeostasis

To investigate the role of *Dlg1* in the mouse adult intestine, we conditionally deleted *Dlg1* throughout the intestinal epithelium using *Vil*^{CreERT2};*Dlg1*$^{FL/FL}$ (*Dlg1*$^{FL/FL}$) mice[54,55] (Figures S1A–S1C″). In addition, to specifically delete *Dlg1* in ISCs, we used *Lgr5*$^{eGFP\text{-}CreERT2}$;*Dlg1*$^{FL/\Delta}$ (*Dlg1*$^{FL/\Delta}$) mice[3,56] in which mosaic recombination takes place in LGR5$^+$ ISCs (Figures S1D–S1E″). Both genetic models generate DLG1$^-$ cells. In control mice, *Dlg1* mRNA was expressed and the protein was basolaterally localized in intestinal epithelial cells (Figures S1A, S1B–S1B″, and S1D–S1D″). After a single tamoxifen induction, *Dlg1* expression was lost at 7 days (Figure S1A); DLG1 protein was completely absent from the epithelium in *Dlg1*$^{FL/FL}$ mice (Figures S1C–S1C″) and diminished in *Dlg1*$^{FL/\Delta}$ mice (Figures S1E–S1E″). To assess the requirement of DLG1 for the maintenance of intestinal epithelial cell polarity, we analyzed membrane distribution of key proteins involved in cell adhesion that mediate cell polarity, including basally located hemidesmosomes by staining β4-integrin (Figures 1A–1C), basolateral adherens junctions by staining E-cadherin (Figures 1D and 1E), and apically localized Ezrin (Figures 1F and 1G).[57–62] Surprisingly, the conditional deletion of *Dlg1* in *Vil*^{CreERT2} mice did not affect the cellular distribution of β4-integrin, E-cadherin, or Ezrin, whereas in all other tissues that have been examined, diminished *Dlg1* expression resulted in impaired cell polarity.[43,56,63–66] Furthermore, the conditional deletion of *Scribble* in the intestinal epithelium leads to disrupted crypt apicobasal polarity and the hyperproliferation of crypt cells.[46] Thus, we next sought to explore whether other crypt functions were disrupted by the loss of *Dlg1* in the intestine. Although the loss of *Dlg1* results in cell fate abnormalities in other tissues,[43,56,66] we found that DLG1 is not required for differentiation into goblet cells, tuft cells, Paneth cells, enteroendocrine cells, and enterocytes (Figures 1H–1V). In addition, we observed no significant difference in the frequency of crypt cell death between controls and DLG1$^-$ intestines (Figures 1W–1Y). Similarly, the number of crypt cells that actively incorporated EdU over the course of 2 h was not significantly different between controls and *Dlg1*$^{FL/\Delta}$ mice (Figures 1Z–1c). Finally, we analyzed the distance that cells moved toward the villus tips over 24 h by injecting control and *Dlg1*$^{FL/FL}$ mice with EdU and BrdU at 48 and 24 h, respectively, before tissue analysis (Figure 1d). Measuring the distance between the leading EdU$^+$ and BrdU$^+$ cells revealed a similar rate of cell displacement in control and DLG1$^-$ intestines (Figures 1e–1g). Thus, in contrast to previous observations showing a requirement for DLG1 in mammalian tissue polarity, the loss of *Dlg1* expression during homeostasis does not affect polarity, integrity, or the ability of the intestinal epithelium to renew.

Wnt signaling activation leads to increased cell death in crypts lacking *Dlg1*

Previous reports showed that loss-of-function mutations in the *Dlg* family of genes contribute to tumorigenesis and inflammatory bowel disease, and these diseases also involve upregulated Wnt signaling.[51,67–73] Therefore, we asked whether DLG1 regulates the response of the intestinal epithelium to elevated Wnt signaling

(R–V) Quantification of intestinal cell populations. n = 5 × 30–40 villi, or 10 crypts per condition, mean ± SD, unpaired t test with Welch's correction.
(W and X) Immunofluorescence images of anti-CC3. Scale bars, 20 μm.
(Y) Quantification of cleaved caspase-3 in crypt region. n = 5 × 10 crypts per condition, mean ± SD, unpaired t test with Welch's correction.
(Z) Experimental schematic for analyzing incorporation of EdU by crypt cells.
(a and b) Immunofluorescence images of EdU. Scale bars, 20 μm.
(c) Quantification of EdU incorporation by crypt cells. n = 3 × 50 crypts per condition, mean ± SD, unpaired t test with Welch's correction.
(d) Experimental schematic for analyzing the migration of crypt cells toward the villus tip.
(e and f) Immunofluorescence images of EdU and anti-BrdU. Arrowheads indicate the leading EdU$^+$ cell (white) and BrdU$^+$ cell (magenta). Scale bars, 50 μm.
(g) Quantification of epithelial cell migration toward villus tip by measuring the distance between leading EdU$^+$ and BrdU$^+$ cells. n = 3 × 50 villi per condition, mean ± SD, unpaired t test with Welch's correction. Nuclei counterstained with DAPI.

CellPress

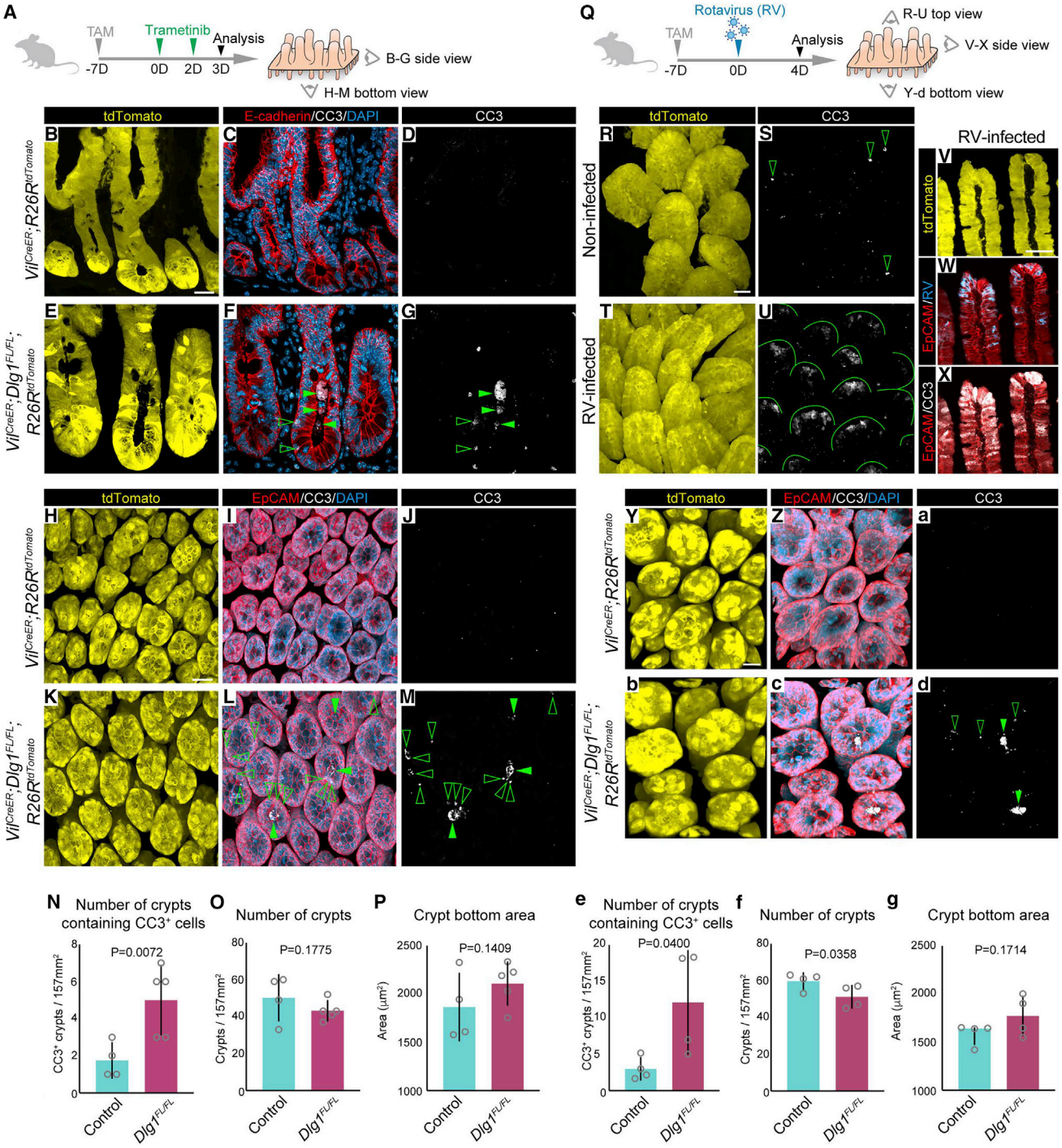

Figure 2. Wnt signaling activation *in vivo* by trametinib or rotavirus leads to increased cell death in crypts lacking DLG1

(A) Experimental schematic for analyzing the epithelial response to trametinib-driven increased Wnt signaling. Mice were injected with one dose of TAM on day 7 followed by two doses of trametinib on days 0 and 2 prior to sacrifice on day 3.

(B–G) Side view of crypts.

(H–M) Bottom view of crypts.

(B, E, H, and K) Images of endogenous tdTomato.

(C, F, I, and L) Immunofluorescence images of anti-E-cadherin or anti-EpCAM with anti-CC3.

(D, G, J, and M) Immunofluorescence images of anti-CC3 with highlighted $CC3^+$ dying cells in the lumen (closed arrowhead) and in the epithelium (open arrowhead). Scale bars for side view images, 20 μm, and for bottom view images, 30 μm.

(N) Quantification of crypts containing $CC3^+$ cells per 157 mm^2 field of view.

(legend continued on next page)

by treating *Vil*^{CreERT2};*Dlg1*$^{FL/FL}$;*R26R*^{tdTomato} (*Dlg1*$^{FL/FL}$;*tdTomato*) mice with intraperitoneal injections of trametinib, a MEK1/2 inhibitor that activates canonical Wnt signaling in the intestine.[74] Mice received two doses of trametinib 7 days after tamoxifen induction, and intestines were isolated 3 days after initial trametinib treatment (Figure 2A). Following this paradigm, we confirmed the activation of canonical Wnt signaling downstream target genes in crypts (Figure S2A). Whole-mount and tissue section analysis of small intestines demonstrated robust Cre recombination in the epithelium, assessed by tdTomato expression (Figures 2B, 2E, 2H, and 2K). The overall intestinal morphology was preserved in trametinib-treated control and DLG1$^-$ mice, but we observed an accumulation of apoptotic cells in the luminal space of DLG1$^-$ crypts, as indicated by labeling with cleaved caspase-3 (CC3) compared with controls (Figures 2B–2N). In images of whole-mounted tissue, we found that dying cells were concentrated also in the epithelium of DLG1$^-$ crypts (Figures 2G and 2M; Videos S1A and S1B). However, the number of crypts remained the same as in control intestines (Figure 2O), and control and DLG1$^-$ crypts showed a similar crypt bottom area (Figures 2P and S2B–S2C).

To further test for the requirement of DLG1 in ISCs when exposed to Wnt signaling upregulation, we next used the enteric pathogen, rotavirus (RV). RV infects and induces cell death of differentiated villus tip cells, while ISCs remain intact.[17,75–77] RV-induced damage promotes canonical Wnt signaling activation in crypts leading to ISC proliferation and differentiation.[17] Mice received a single RV inoculation via oral gavage 7 days after tamoxifen induction, and intestines were isolated 4 days after infection at the peak of viral shedding (Figure 2Q).[17] Fecal pellets were collected for ELISA to confirm RV viral load on day 4 post-infection (Figure S2D). We collected whole-mount tissue to assess RV-induced damage. We observed robust CC3 staining extending the length of villus tips in infected intestines (Figures 2R–2U). As expected, infected cells were specifically localized to the tip of the villi and colocalized with the staining of CC3 (Figures 2V–2X). Similar to trametinib, RV-induced Wnt signaling activation promoted the accumulation of dying cells in DLG1$^-$ crypts (Figures 2Y–2e; Videos S2A and S2B). Unlike trametinib treatment, RV infection led to a significant decrease in the number of crypts of DLG1$^-$ intestines compared with controls (Figure 2f). In both trametinib and RV, the remaining crypts in DLG1$^-$ intestines had a similar crypt bottom area as controls (Figure 2g). Taken together, these results show that high levels of Wnt signaling trigger increased cell death in epithelial crypts lacking DLG1.

Elevated levels of canonical Wnt ligands promote rapid loss of DLG1$^-$ organoids

Intestinal organoids enable the functional dissection of how specific niche signals affect the epithelium. To determine if the increase in cell death *in vivo* was linked to the response of ISCs to Wnt signaling, we generated intestinal organoids from control and *Dlg1*$^{FL/FL}$;*tdTomato* intestines and exposed them to exogenous WNT3A conditioned medium (WNT3A CM) (Figure 3A) or recombinant WNT3A (Figure S3I). Exogenous Wnt ligands in organoids mimic tissue regeneration, which is reflected by increased expression of fetal ISC markers like *Lgr4*, *Birc5*, *Ly6a*, and *Cnx43* (Figures S3A–S3D) and a sharp decrease of adult ISC markers *Lgr5* and *Olfm4* (Figures S3E and S3F).[78–81] The loss of expression of *Lgr5* and *Olfm4* was accompanied by decreased expression of their regulator *Ascl2* (Figure S3G). Additionally, after exogenous Wnt exposure, organoids morphologically change from budding crypts to spheroids that are composed of hyperproliferative ISCs.[11,79,82,83] Organoids were passaged by cell dissociation, then treated with 4-hydroxytamoxifen (4-OHT) to genetically ablate *Dlg1* (Figure S3H), and concurrently exposed to 50% WNT3A CM (Figure 3A). Between 24 and 144 h, control cells formed spheroids and continued growing, whereas the majority of DLG1$^-$ cells did not give rise to spheroids, and the few spheroids that formed remained significantly smaller than controls (Figures 3B–3H). We observed the same behavior in DLG1$^-$ crypts when they were treated with 200 ng/mL of recombinant WNT3A (Figure S3I), demonstrating that treatment with WNT3A alone is sufficient to reveal this distinction between the wild-type and DLG1$^-$ organoids (Figures S3J–S3P). Next, we analyzed the effect of increasing levels of Wnt CM, ranging from 0.5% to 20% on wild-type or DLG1$^-$ organoids. All tested concentrations supported the spheroid growth of control organoids with no apparent difference between the size of the spheroids in 0.5% to 20% of WNT3A CM, suggesting that even low amounts of Wnt are sufficient to drive the regenerative response (Figures S4A–S4D and S4I–S4M). By contrast, the vast majority of DLG1$^-$ organoids could not grow as spheroids at any WNT3A CM concentration

(O) Quantification of the number of crypts per 157 mm^2 field of view.
(P) Quantification of crypt bottom area. n = 4–5 × 10 fields of view per condition, mean ± SD, unpaired t test with Welch's correction.
(Q) Experimental schematic for analyzing the epithelial response to rotavirus (RV) infection.[17] Mice were injected with one dose of TAM on day 7 followed by rotavirus infection on day 0 prior to sacrifice on day 4.
(R–U) Top view of villi.
(V–X) Side view of villi.
(Y–d) Bottom view of crypts.
(R, T, V, Y, and b) Images of endogenous tdTomato.
(S and U) Immunofluorescence images of anti-CC3 with highlighted CC3$^+$ dying cells in villi tips of control mice (open arrowheads) and RV-infected mice (lines).
(W and X) Immunofluorescence images of anti-Epcam with anti-RV or anti-CC3.
(Z and c) Immunofluorescence images of anti-EpCAM and anti-CC3.
(a and d) Immunofluorescence images of anti-CC3 with highlighted CC3$^+$ dying cells in the lumen (closed arrowhead) and in the epithelium (open arrowhead). Scale bar for top and side view images, 50 μm, and for bottom view images, 20 μm.
(e) Quantification of crypts containing CC3$^+$ cells per 157 mm^2 field of view.
(f) Quantification of the number of crypts per 157 mm^2 field of view.
(g) Quantification of crypt bottom area. n = 4 × 6 fields of view per condition.
(e and f) Mean ± SD, unpaired t test with Welch's correction.
(g) median ± interquartile range, unpaired Mann-Whitney test. Nuclei counterstained with DAPI.

CellPress

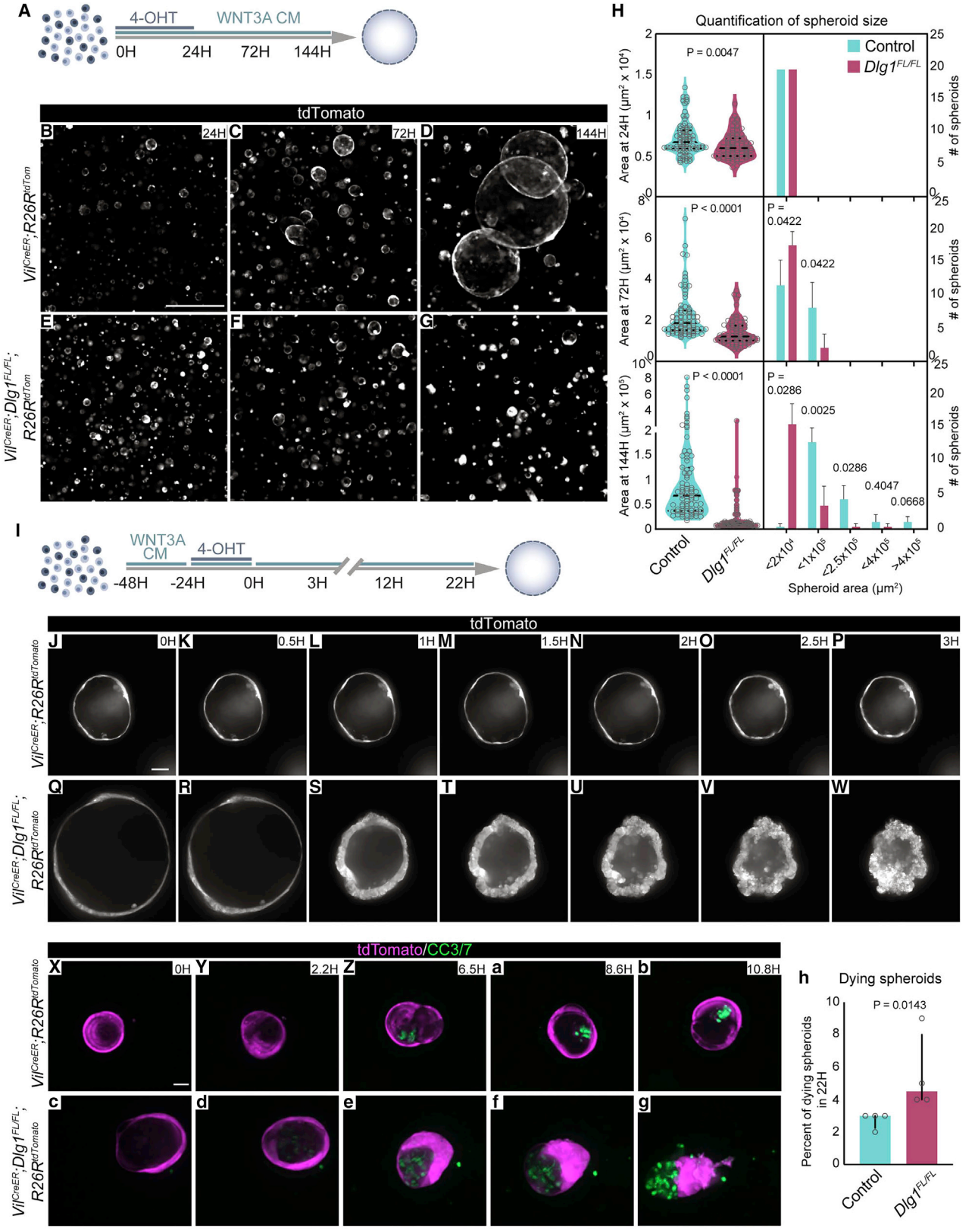

(legend on next page)

(Figures S4E–S4H and S4I–S4M), confirming that *Dlg1* is critical for proper ISC response during increased levels of Wnt signaling.

In addition to epithelial-derived WNT3A, ISCs are continuously exposed to mesenchymal-derived canonical and non-canonical Wnt ligands. We asked whether the impaired response of DLG1$^-$ ISCs is attributed solely to WNT3A or whether this phenotype can be observed with other Wnt ligands. Crypts from control and *Dlg1*$^{FL/FL}$;*tdTomato* intestines were grown in a conditioned medium of niche PDGFRα^{lo} cells (PDGFRα^{lo} CM) or 500 ng/mL of non-canonical recombinant WNT5A (Figure S4N). PDGFRα^{lo} CM contains canonical WNT2B and WNT9A, and similarly to WNT3A, CM promotes the rapid transformation of organoids into spheroids.[84] At 72 h the majority of control crypts grew as spheroids (Figures S4O, S4P, and S4S), whereas DLG1$^-$ crypts responded poorly, and only a fraction of seeded crypts initiated spheroid growth (Figures S4Q–S4S). Similar to the WNT3A treatment, DLG1$^-$ spheroids were significantly smaller compared with controls (Figure S4T). However, in contrast to treatment with WNT3A or canonical ligands derived from PDGFRα^{lo} cells (Figures S3P and S4T), we observed no significant difference in the number or size of spheroids that were formed between DLG1$^-$ and control crypts exposed to non-canonical WNT5A (Figures S4U–S4Z). In agreement with previous reports, WNT5A promoted short-term *in vitro* survival but not rapid growth as observed with canonical Wnts, and organoids eventually died after 5 days in culture (data not shown).[15,85] Overall, these data indicate that DLG1 is required for the normal response of ISCs to high levels of multiple Wnt ligands, but the capacity to respond to non-canonical WNT5A is DLG1 independent.

Next, we explored if endogenous levels of WNT3A coming from Paneth cells are sufficient to phenocopy the loss of organoids observed in increased levels of WNT3A. Therefore, we established organoids from control *Lgr5*$^{eGFP\text{-}CreERT2}$;*Dlg1*$^{FL/WT}$;*R26R*^{tdTomato} (*Dlg1*$^{FL/WT}$;*tdTomato*) and mutant *Lgr5*$^{eGFP\text{-}CreERT2}$;*Dlg1*$^{FL/\Delta}$;*R26R*^{tdTomato} (*Dlg1*$^{FL/\Delta}$;*tdTomato*) mice that had been induced with a single dose of tamoxifen 14 days prior to organoid establishment (Figure S5A). The mosaic nature of *Lgr5*$^{eGFP\text{-}CreERT2}$[3] results in the presence of both tdTomato$^-$/DLG1$^+$ and tdTomato$^+$/DLG1$^-$ organoids within the same well. This enabled a comparison of the fraction of live cells between tdTomato$^-$/DLG1$^+$ and tdTomato$^+$/DLG1$^-$ organoids by flow cytometry (Figure S5B). In both *Dlg1*$^{FL/WT}$;*tdTomato* and *Dlg1*$^{FL/\Delta}$;*tdTomato* organoids, the tdTomato$^+$ cells persisted over 47 days (Figure S5C). Even though we observed a slow decline in the numbers of tdTomato$^+$/DLG1$^-$ cells, the decrease was negligible compared with the inability to grow observed in high Wnt. qPCR analysis of *Dlg1*$^{FL/\Delta}$;*tdTomato* organoids revealed that loss of *Dlg1* expression did not affect the expression of major epithelial differentiation markers between tdTomato$^-$/DLG1$^+$ and tdTomato$^+$/DLG1$^-$ organoids (Figures S5D–S5F). In summary, the loss of DLG1$^-$ organoids positively correlates with the levels of WNT3A that they are exposed to and is not a consequence of impaired cell differentiation.

High Wnt conditions promote ISC death in the absence of *Dlg1*

Based on our finding that single cells lacking *Dlg1* fail to form spheroids when exposed to exogenous Wnt, we asked whether single cells expressing *Dlg1* grow into spheroids and collapse only when they lose DLG1. To test this hypothesis, control and non-induced mutant single cells were grown in high Wnt conditions for 24 h. Once spheroids formed, *Dlg1* ablation was induced by a 24 h pulse of 4-OHT, followed by a 3 or 22 h imaging (Figure 3I). Both control and non-induced mutant single cells were able to grow into spheroids when exposed to WNT3A CM (Figures 3J and 3Q). However, DLG1$^-$ spheroids transitioned from thin-walled spheroids to progressively smaller, amorphous, and thick-walled structures, whereas the morphology of control spheroids was unperturbed (Figures 3J–3W; Videos S3A and S3B). As DLG1$^-$ spheroids ultimately collapsed, cells that remained within the epithelium became more cuboidal than slender, and cells that had left the epithelium rounded up and accumulated on the basal and apical sides of the epithelium. Together, these events caused the visual effect of epithelial "wall" thickening.

Finally, we asked if the DLG1$^-$ spheroid growth phenotype was due to impaired proliferation and/or increased cell death. EdU incorporation demonstrated that DLG1$^-$ spheroids had no apparent proliferative defect (Figures S5G–S5N). To test for cell death, we live imaged the spheroids for up to 12 h in the presence of cleaved caspase-3/7 dye (CC3/7). Control organoids accumulated only small amounts of fluorescence coming from the CC3/7 reporter dye in the spheroid lumen over 12 h (Figures 3X–3b and 3h; Video S4A). By contrast, DLG1$^-$ spheroids accumulated increasing amounts of CC3/7$^+$ cells and eventually collapsed (Figures 3c–3h; Video S4B). Together, the *in vivo* and *in vitro* data indicate that, instead of initiating a regenerative response following increased Wnt signaling, ISCs lacking DLG1 undergo cell death.

Transcription of CDC42 GTPase-activating protein (*Arhgap31*) is reduced following *Dlg1* loss in ISCs

To determine the molecular mechanism responsible for increased epithelial apoptosis in response to WNT3A, we analyzed the transcriptional profile of the DLG1$^-$ ISCs. To delete

Figure 3. Genetic deletion of *Dlg1* leads to ISCs death in high WNT3A conditions

(A) Experimental schematic for analyzing the ISC response to increased WNT3A levels. Organoids were dissociated into single cells that were treated with ENR medium containing 4-hydroxy-tamoxifen (4-OHT) and WNT3A conditioned medium (WNT3A CM).

(B–G) Images of endogenous tdTomato expressing spheroids at (B and E) 24 h, (C and F) 72 h, and (D and G) 144 h after plating. Scale bars, 500 μm.

(H) Quantification of spheroid size by binning them according to the area at 24, 72, and 144 h after plating. n = 4 organoid lines per condition. Area at all time points: median ± interquartile range, unpaired Mann-Whitney test. # spheroids at 72 h: mean ± SD, unpaired t test with Welch's correction. # spheroids at 144 h: median ± interquartile range, unpaired Mann-Whitney test.

(I) Experimental schematic for analyzing DLG1 requirement in control or DLG1$^-$ organoids exposed to increased WNT3A levels. Single cells were exposed to WNT3A CM for 24 h to let them grow into spheroids. Then, spheroids were treated with 4-OHT for 24 h and imaged for 3–22 h.

(J–W) Frames from time-lapse imaging of spheroids expressing tdTomato report. Scale bars, 50 μm.

(X–g) Frames from time-lapse imaging of spheroids expressing tdTomato report and incubated with CC3/7 dye prior to and during live imaging. Scale bars, 20 μm.

(h) Quantification of the number of dying spheroids. n = 4 organoid lines per condition, median ± interquartile range, unpaired Mann-Whitney test.

CellPress

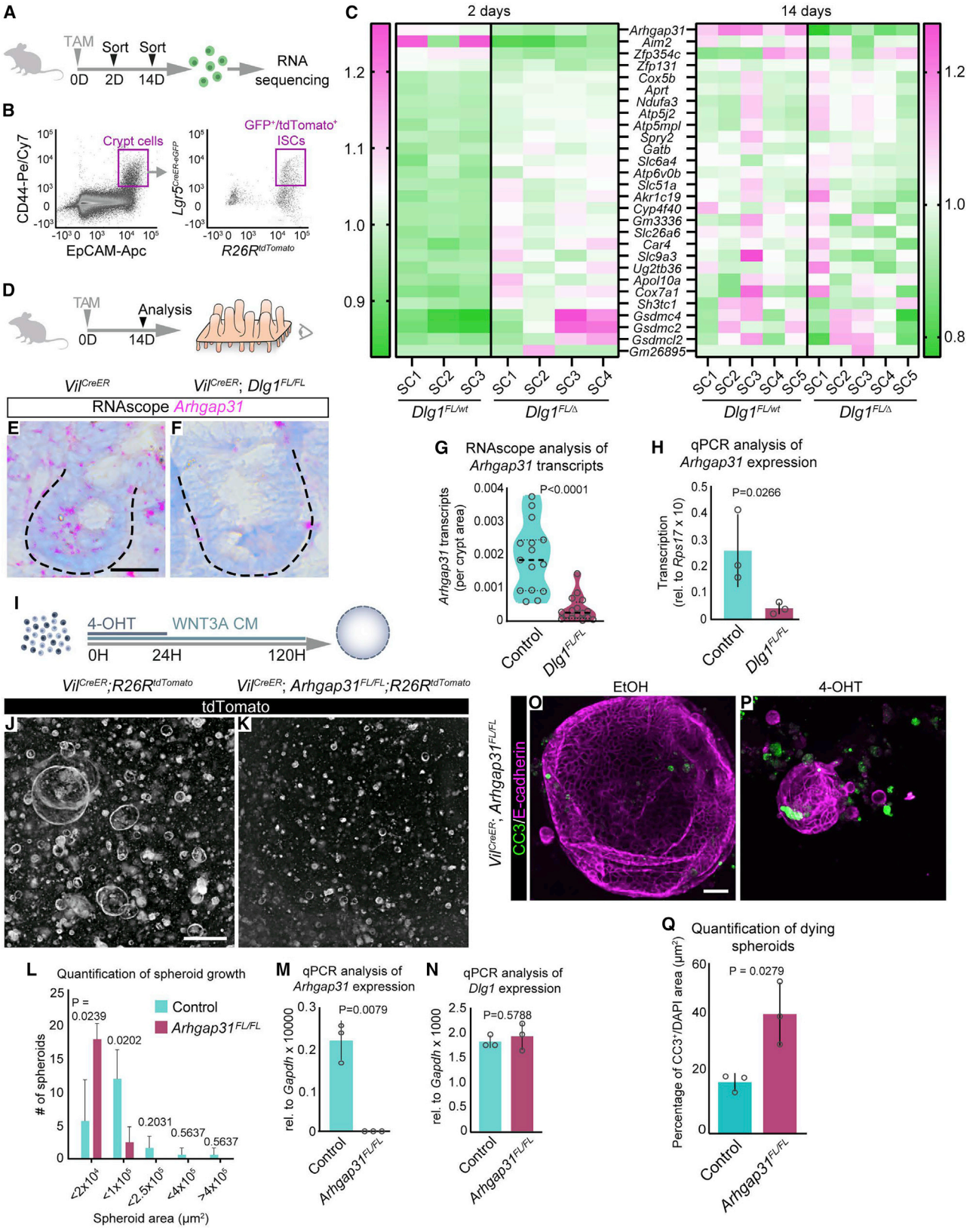

(legend on next page)

Dlg1 in ISCs, *Dlg1*$^{FL/WT}$;*tdTomato* and *Dlg1*$^{FL/\Delta}$;*tdTomato* mice were given 1 dose of tamoxifen. Recombined ISCs lacking *Dlg1* were isolated by FACS (DAPI$^-$/EpCAM$^+$/CD44$^+$/*Lgr5*-eGFP$^+$/tdTomato$^+$) and their actively transcribed genes were assessed by RNA sequencing. To identify changes intrinsic to ISCs as well as changes influenced by the DLG1$^-$ microenvironment, we analyzed ISCs at 2 and 14 days after induction (Gene Expression Omnibus GSE198573) (Figures 4A and 4B). Surprisingly, the only gene that was differentially expressed at both 2 and 14 days was *Arhgap31*, a CDC42 GTPase-activating protein (Figure 4C). We identified another 27 genes with differential expression in *Dlg1*$^{FL/\Delta}$ ISCs at the 2-day time point, but none of them were significantly up- or down-regulated at 14 days (Figure 4C). At 14 days after tamoxifen-induced *Dlg1* loss (Figure 4D), the downregulation of *Arhgap31* occurred throughout the entire epithelium, as indicated by mRNA quantification using RNAscope and by qPCR of sorted intestinal epithelial cells (DAPI$^-$/EpCAM$^+$) (Figures 4E–4H).

Next, we asked if the phenotype observed in DLG1$^-$ organoids following exposure to exogenous WNT3A was driven by the transcriptional downregulation of *Arhgap31* in DLG1$^-$ ISCs. We induced the recombination of *Vil*^{CreERT2};*Arhgap31*$^{FL/FL}$;*R26R*^{tdTomato} (*Arhgap31*$^{FL/FL}$;*tdTomato*) organoids and treated them with WNT3A CM for 6 days (Figure 4I). Similar to DLG1$^-$ cells, ARHGAP31$^-$ cells responded poorly to exogenous WNT3A and failed to form viable spheroids (Figures 4J–4L). Importantly, the deletion of *Arhgap31* did not affect the expression of *Dlg1* (Figures 4M and 4N), suggesting that DLG1 acts upstream of ARHGAP31. Additionally, we found that under high Wnt conditions, ARHGAP31$^-$ spheroids underwent cell death, phenocopying DLG1$^-$ spheroids (Figures 4O–4Q).

To analyze the dynamics of ARHGAP31$^-$ organoids in media containing only Paneth cell-derived WNT3A, we established organoids from control and *Arhgap31*$^{FL/FL}$;*tdTomato* and treated them with ethanol (EtOH) or 4-OHT for 48 h. Following passaging, tdTomato$^-$/ARHGAP31$^+$ and tdTomato$^+$/ARHGAP31$^-$ crypts were mixed together, and the ratio of tdTomato$^-$ and tdTomato$^+$ cells was quantified by flow cytometry for 5 passages (Figure S6A). As with tdTomato$^+$/DLG1$^-$ organoids (Figure S3Q), tdTomato$^+$/ARHGAP31$^-$ organoids (Figure S6B) persisted over 40 days in culture (Figure S6C). Taken together, these data show that the loss of *Dlg1* reduces *Arhgap31* expression and that DLG1 acts upstream of ARHGAP31, which is important when levels of Wnt signaling are increased.

Reduced ARHGAP31 expression leads to the activation of CDC42, which negatively impacts ISC migration and cell division

ARHGAP31 deactivates a downstream activator of the Wnt-planar cell polarity (PCP) pathway, CDC42, by promoting the hydrolysis of GTP.[86,87] Since we found that *Arhgap31* expression was reduced in DLG1$^-$ intestinal epithelium, we hypothesized that CDC42 activity would be elevated in DLG1$^-$ ISCs. To test this hypothesis, we established and treated control and *Dlg1*$^{FL/FL}$ organoids with 4-OHT and measured the levels of active CDC42 in sorted cells (Figure 5A). In order to obtain a sufficient number of DLG1$^-$ cells for quantification of CDC42-GTP, we used organoids instead of spheroids because DLG1$^-$ spheroids have a rapid decline in cell numbers caused by cell death. Using the G-LISA assay to measure the active GTP-bound form of CDC42 in FACS-sorted DLG1$^+$ and DLG1$^-$ cells, we found that the intracellular level of active GTP-CDC42 was significantly increased in DLG1$^-$ organoids compared with DLG1$^+$ organoids (Figure 5B). Interestingly, the intracellular level of active RAC1, another target of ARHGAP31,[86] was not altered in DLG1$^-$ cells compared with control organoids (Figure 5C).

ARHGAP31, through its regulation of CDC42 activity, is involved in cellular motility, migration, and proliferation.[88] In particular, high levels of ARHGAP31 are oncogenic, promoting cell migration and invasion.[89] To examine if loss of DLG1 with the subsequent reduction of ARHGAP31 and increased active CDC42 affects ISC cellular behaviors such as migration, we evaluated ISC motility and migration using a scratch wound assay. To simplify the 3D architecture of spheroids and facilitate the analysis of ISC migration, we cultured *Vil*^{CreERT2};*R26R*^{mTmG} or *Vil*^{CreERT2};*Dlg1*$^{FL/FL}$; *R26R*^{mTmG} (*Dlg1*$^{FL/FL}$;*mTmG*) intestinal monolayers[90] in the presence of WNT3A CM and 4-OHT (Figure 5D). The WNT3A treatment of 2D monolayers results in the

Figure 4. *Arhgap31* expression is regulated by DLG1 in ISCs

(A) Experimental schematic for identifying differentially expressed genes in DLG1$^-$ ISCs. Mice were injected with 1 dose of TAM, and 2 or 14 days later ISCs were isolated by FACS-sorting, and mRNA was sequenced.

(B) Flow cytometry plot showing gating strategy for sorting specifically ISCs.

(C) Heatmap showing relative expression of genes at 2 and 14 days in control and DLG1$^-$ ISCs. Since *Arhgap31* was the only differentially expressed gene at 14 days, to generate the 14-day heatmap, we used the remaining 27 genes that were identified to be differentially expressed at 2 days. Gene expression in DLG1$^-$ samples are displayed as a fraction of expression in DLG$^+$ normalized across all samples. SC, stem cells isolated from individual mice.

(D) Experimental schematic for analyzing *Arhgap31* transcripts in intestinal crypts. Mice were injected with one dose of TAM 2 weeks prior to sacrifice.

(E and F) RNAscope images of *Arhgap31* expression in (E) DLG1$^+$ and (F) DLG1$^-$ crypts. Scale bars, 25 μm.

(G) Quantification of *Arhgap31* transcripts in crypt regions normalized to crypt areas. n = 3 × 5 crypts per condition, median ± interquartile range, unpaired Mann-Whitney test.

(H) Transcription levels of *Arhgap31* in intestinal epithelial cells analyzed by qPCR. n = 3 mice per condition, mean ± SD, unpaired t test with Welch's correction.

(I) Experimental schematic for analyzing the ISC response to increased WNT3A levels in ARHGAP31$^-$ spheroids.

(J and K) Images of endogenous tdTomato expressing (J) ARHGAP31$^+$ and (K) ARHGAP31$^-$ spheroids grown in the presence of WNT3A CM for 120 h. Scale bars, 500 μm.

(L) Quantification of spheroid by binning them according to size at 120 h. n = 3–4 organoid lines, per condition, mean ± SD, unpaired t test with Welch's correction.

(M and N) Transcription levels of *Arhgap31* and *Dlg1* analyzed by qPCR on FACS-sorted live intestinal organoids (DAPI$^-$). n = 3, per condition, mean ± SD, unpaired t test with Welch's correction.

(O and P) Immunofluorescence images of anti-CC3-stained and anti-E-cadherin-stained spheroids treated with (O) ethanol (EtOH) or (P) 4-OHT. Scale bars, 50 μm.

(Q) Quantification of the number of dying spheroids. n = 3 organoid lines per condition, mean ± SD, unpaired t test with Welch's correction.

CellPress

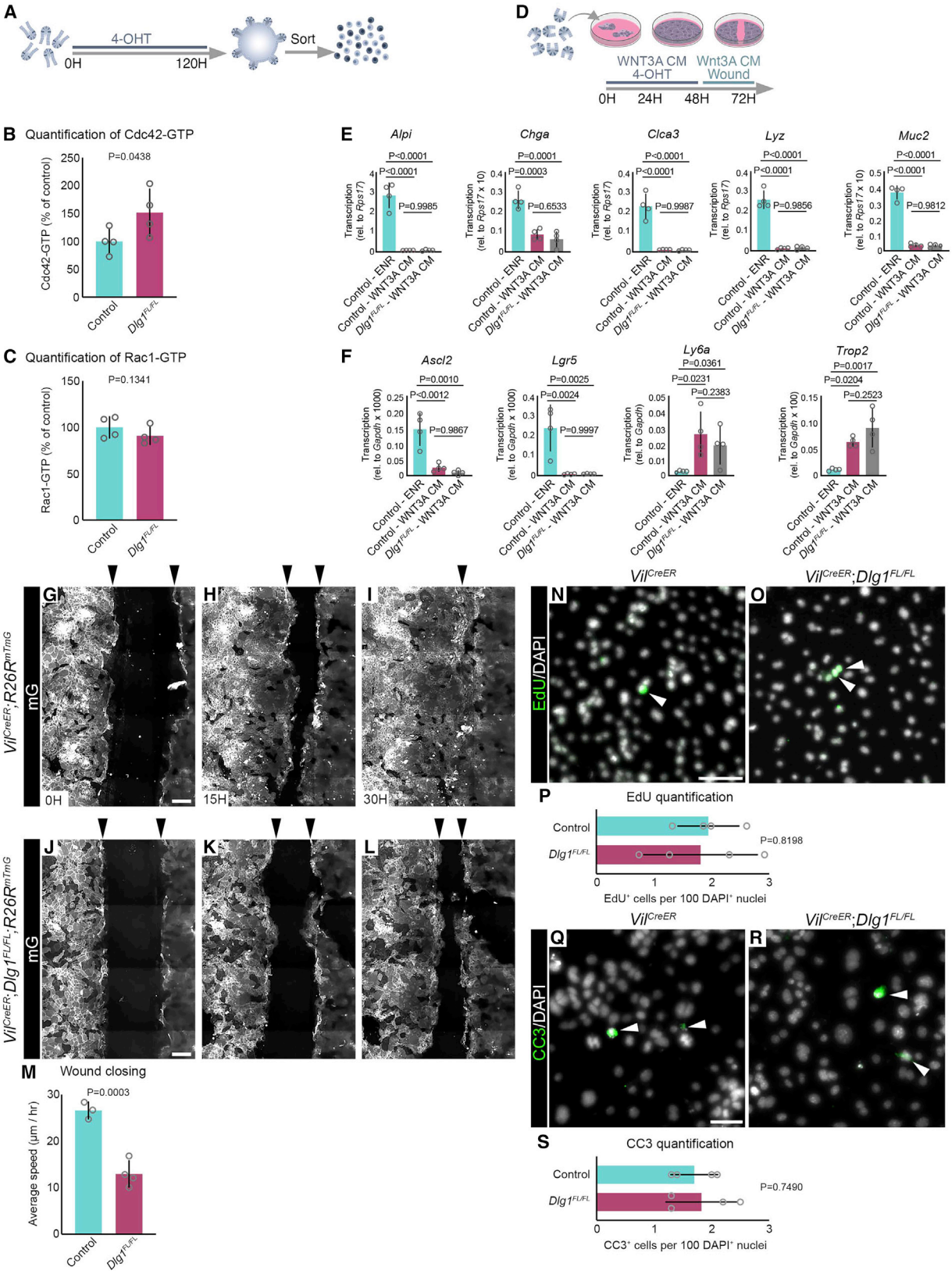

(legend on next page)

depletion of differentiated cells as quantified by qPCR (Figure 5E). As with spheroids, 2D monolayers expressed a genetic profile associated with regeneration and fetal ISCs (Figure 5F). After the cells reached confluence, we scratched the ISC monolayers to create a wound spanning the entire culture plate and measured the time it took to close the wound. mG$^+$/DLG1$^+$ ISC monolayers closed the wound at 30 h after scratching (Figures 5G–5I; Video S5A), whereas mG$^+$/DLG1$^-$ ISC monolayers failed to close the wound (Figures 5J–5L; Video S5B). On average, control mG$^+$/DLG1$^+$ ISC monolayers moved at 27 μm/h, and mutant mG$^+$/DLG1$^-$ ISC monolayers were significantly slower, at 13 μm/h (Figure 5M). To determine if the difference in migration was caused by different rates of proliferation or cell death in the confluent 2D cultures, we quantified EdU$^+$ and CC3$^+$ cell numbers in control and DLG1$^-$ cultures 12 h after the scratch. No difference was observed in the number of proliferating and dying cells between control and DLG1$^-$ cultures (Figures 5N–5S), supporting the idea that DLG1$^-$ ISCs failed to close the wound due to impaired migration.

CDC42 is a well-known regulator of various cellular functions, including motility, cytoskeletal rearrangement, and proliferation.[91,92] In the intestine, the deletion of CDC42 causes stem and TA cell hyperproliferation and crypt hyperplasia.[93] We performed live imaging of DLG1$^-$ organoid crypts to test if active CDC42 impacts cell division. Using *Lgr5$^{eGFP\text{-}CreERT2}$* to delete *Dlg1* in ISCs after 24 h of induction (Figure 6A), we found that cell divisions in control ISCs progressed to completion (Figures 6B–6I; Videos S6A and S6B). However, LGR5$^+$ ISCs lacking DLG1 rounded up, and their cell membrane blebbed (Figures 6J–6Q; Videos S6C and S6D). To better characterize the cellular behavior in DLG1$^-$ crypts, we used the *mTmG* membrane reporter, which allows precise tracking of individual cells. Prior to recombination, *Dlg1$^{FL/FL}$;mTmG* cells were able to divide akin to their control counterparts (Videos S7A and S7B). After a 24 h pulse of 4-OHT resulting in the mosaic deletion of *Dlg1* and mG reporter expression, we followed individual cell divisions (Figure 6R). During crypt cell division, mitotic cells round up, progressively moving toward the apical surface of the epithelium where cytokinesis takes place (Figures 6S–6U; Video S7C). As mitosis ends and interphase begins, daughter cells elongate, occupying the entire apical-basal axis of the epithelium[94] (Figure 6V; Video S7C). In contrast to cell division in recombined control mG$^+$/DLG1$^+$ cells, recombined mutant mG$^+$/DLG1$^-$ dividing cells rounded up but failed to complete mitosis, resulting in blebbing, death, and extrusion (Figures 6W–6e; Video S7D). Together, these findings indicate that loss of *Dlg1* leads to elevated CDC42-GTP in ISCs, impairing cell motility and cell division.

DISCUSSION

The small intestine has the fastest cell turnover rate of all mammalian epithelia,[5] and as such, its renewal relies heavily on niche signals that ensure proper stem cell function. The niche, or cellular microenvironment, provides factors that guide stem cell behavior, including proliferation, differentiation, and polarity.[95] Throughout the life cycle of an organism, niche signals change in activity levels due to external stimuli or diseases, and stem cells need to respond accordingly to fulfill tissue renewal, but how stem cells interpret fluctuating niche signals is not clear. Here, we have elucidated cellular and molecular mechanisms that ISCs use to respond to increased levels of canonical Wnt ligands, which are crucial niche signals for ISCs.[96,97]

ISCs depend on canonical Wnt signaling for homeostatic self-renewal.[19] During intestinal injury, increased canonical Wnt signaling is involved in epithelial regeneration,[17,25–30] whereas the aberrant activation of the pathway causes colorectal cancer.[31] We found that canonical WNT3A participates in the non-canonical PCP pathway via a DLG1-ARHGAP31-CDC42 molecular axis. DLG1 in ISCs is required for a proper response to high WNT3A during regeneration by regulating *Arhgap31* transcription. Increased ARHGAP31 deactivates CDC42, allowing ISC proliferation required for regeneration (Figure 7A). In the absence of DLG1, the regenerative levels of WNT3A become detrimental. Reduced ARHGAP31 causes accumulation of CDC42-GTP, culminating in failed cell division and death (Figure 7B). Furthermore, we confirmed that other canonical Wnt

Figure 5. Loss of *Dlg1* results in increased levels of activated CDC42 followed by impaired cell migration

(A) Experimental schematic for analyzing the active forms of CDC42-GTP and RAC1-GTP in organoids. Organoids were mechanically disrupted into crypts that were treated with ENR medium containing 4-OHT. After 5 days, organoids were then enzymatically dissociated into live single cells (DAPI$^-$) that were FACS-sorted and processed for analyzing CDC42-GTP and RAC1-GTP levels by G-LISA.

(B) Quantification of CDC42-GTP levels in DLG1$^+$ and DLG1$^-$ organoids. n = 4 organoid lines per condition, mean ± SD, unpaired t test with Welch's correction.

(C) Quantification of RAC1-GTP levels in DLG1$^+$ and DLG1$^-$ organoids. n = 4 organoid lines per condition, mean ± SD, unpaired t test with Welch's correction.

(D) Experimental schematic for analyzing the migration capacity of 2D organoid monolayers assessed by scratch wound assay. Organoids were mechanically disrupted into crypts that were plated on Matrigel-coated 24-well plates and treated with ENR medium containing 4-OHT and WNT3A CM and grown for 48 h. After reaching confluency, the center of the well was scratched with a P200 tip and organoids were imaged for 30 h to record the speed of migration in the direction of the scratch.

(E and F) Transcription levels of (E) differentiated cell markers and (F) Wnt target genes analyzed by qPCR from FACS-sorted live (DAPI$^-$) 2D monolayers established from control and DLG1$^-$ mice. n = 4 organoid lines per condition, mean ± SD, one-way ANOVA with Tukey's multiple comparisons test.

(G–L) Frames from time-lapse imaging of 2D organoid monolayers expressing mG. Arrowheads above the images indicate the leading edges of the migrating 2D organoids. Scale bars, 200 μm.

(M) Quantification of the average speed at which organoids migrated in the direction of the scratch/wound. n = 3–4 organoid lines per condition, mean ± SD, unpaired t test with Welch's correction.

(N and O) Immunofluorescence images of EdU stained 2D organoid monolayers at 12 h post-scratch/wound. Scale bars, 50 μm.

(P) Quantification of EdU. n = 4 organoid lines per condition, mean ± SD, unpaired t test with Welch's correction.

(Q and R) Immunofluorescence images of anti-CC3 stained 2D organoid monolayers at 12 h post-scratch/wound. Scale bars, 50 μm.

(S) Quantification of CC3. n = 4 organoid lines per condition, mean ± SD, unpaired t test with Welch's correction. Nuclei counterstained with DAPI.

CellPress

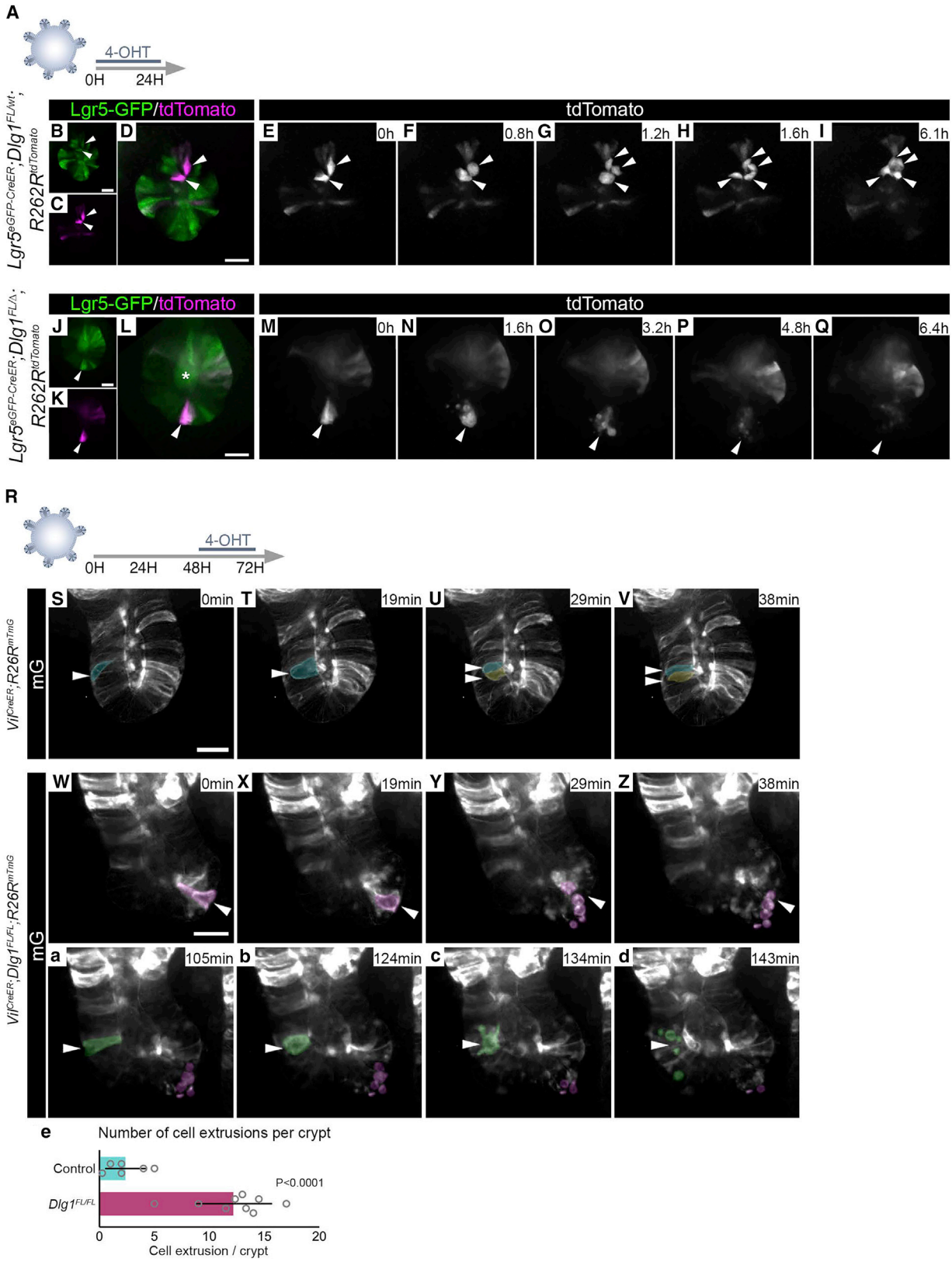

(legend on next page)

ligands, but not the non-canonical WNT5A ligand, mimic the response of WNT3A.

The WNT1 family of ligands, including WNT3A, are components of the canonical Wnt/β-catenin signaling pathway that are ubiquitous promoters of cell proliferation.[98] The non-canonical Wnt/PCP signaling pathway is activated by the WNT5A family of ligands that control polarization of tissues, cell motility, mitosis, and cytoskeletal organization in both healthy and cancerous tissues.[99–102] Crosstalk between canonical and non-canonical Wnt pathways can regulate various cytoskeletal-dependent cellular behaviors in development and homeostasis, such as migration and adhesion.[103–107] In particular, WNT3A can activate non-canonical signaling in osteoblasts, chondrocytes, mesenchymal stem cells, and colon cancers.[108–111] Our findings demonstrate an intersection between the canonical WNT3A ligand and non-canonical Wnt/PCP output and suggest a previously unrecognized mechanism that underlies ISC-driven intestinal regeneration, and we propose that ISCs, once exposed to upregulated WNT3A, require DLG1 for replication. In the context of *Dlg1* loss, Wnt/β-catenin target genes in ISCs are transcriptionally unchanged compared with ISCs in control intestines that are exposed to normal Wnt levels. Additionally, in DLG1$^-$ ISCs, the only differentially expressed gene at both 2 and 14 days was *Arhgap31*, which regulates the non-canonical Wnt-PCP pathway. Together, these findings raise the intriguing possibility that WNT3A can simultaneously activate canonical and non-canonical Wnt pathways in ISCs.

Prior studies in organisms ranging from *Drosophila* to mammals have shown the essential role of DLG1 as a member of the Scribble protein complex in maintaining the apicobasal polarity of epithelial cells.[112] However, we found that, after the conditional deletion of *Dlg1* in the homeostatic adult small intestine, crypts exhibited normal polarity protein localization and cell proliferation. Furthermore, the distance of cell displacement, used as a measure of the speed by which older cells are pushed along the crypt-villus axis by new daughter cells, is unchanged in DLG1$^-$ crypts. From these results, we conclude that cell polarity and polarity-dependent phenotypes like cell division are not affected by the loss of *Dlg1* under homeostatic Wnt signaling regimes. This may be due to redundancy between *Dlg* vertebrate paralogs that is sufficient for the maintenance of adult intestinal epithelium cell polarity in mammals or because polarity is controlled by other factors such as the integrin adhesion complex. Our data complement a study in *Drosophila* showing that, unlike other fly epithelia, midgut cell polarity is controlled by factors other than the classical Scribble polarity complex.[47] In addition, a prior report demonstrated that *Dlg1* deletion at embryonic day 9 did not affect polarity in adult mouse intestinal epithelium *in vivo* and *in vitro*.[51] However, our results contrast with the latter report regarding delayed cell displacement from crypts. These conflicting results may be due to the constitutive genetic system used in the previous report versus our conditional genetic system.

Our data support a model in which ISC proliferation and motility during regeneration is under the control of CDC42 inactivation by ARHGAP31 (Figure 7). Consistent with this model, ARHGAP31 has been identified as a GAP for CDC42, and CDC42 is a critical regulator of cell motility.[86,88] Furthermore, the depletion of ARHGAP31 in prostate cancer cells significantly reduced their cytoskeletal-dependent phenotypes, like migration and invasion.[89] This molecular model may be a conserved mechanism of non-canonical Wnt directed cell migration, as it has been shown that non-canonical Wnt signaling promotes ISCs movement to sites of injury in the *Drosophila* intestine.[113] Aging ISCs have elevated CDC42 activity and reduced regenerative capacity.[114] Experimentally, an increase of activated CDC42 accelerated ISC aging, whereas a decrease of CDC42 activity enhanced the regenerative capacity of aged ISCs.[114] This raises the intriguing possibility that the molecular mechanism that we describe during regeneration is impaired in aging ISCs.

A key finding from our live imaging is that Dlg1$^-$ ISCs undergo cell death while they try to divide. We observed that mutant cells die at the apical surface of the epithelium, suggesting that failed apical mitosis triggers cell extrusion and death. In *C. elegans* embryos, S phase arrest during the cell cycle ends in cell elimination via extrusion,[115] suggesting that cell death promoted by cell division stress is an evolutionarily conserved mechanism. Nonetheless, it is unclear if the observed cell division failure is a direct consequence of the loss of DLG1 at the midbody during cytokinesis,[116] a CDC42-dependent cytoskeletal rearrangement,[117–119] or both. A parallel molecular axis in the Wnt-PCP pathway that phenocopies our observations in cell replication, survival, and motility is RhoA-ROCK. The genetic deletion of RhoA results in cytokinesis failure, leading to cell cycle arrest culminating in cell death. Furthermore, RhoA deletion impairs cellular chemotaxis.[120] It remains to be explored whether DLG1 can function via the RhoA-ROCK axis and whether decreased motility and increased cell death resulting from loss of *Dlg1* contribute to impaired regeneration by independent mechanisms.

Figure 6. ISCs fail to divide and undergo cell death in the absence of *Dlg1*

(A) Experimental schematic for analyzing the cell division of ISCs. Organoids grown in ENR medium for 48 h were treated with 1 μM 4-OHT for 24 h prior to live imaging.

(B–Q) Frames from time-lapse imaging of organoid crypts expressing tdTomato and Lgr5-GFP. (B–I) Recombined tdTomato$^+$/Lgr5-GFP$^+$ ISCs dividing in DLG1$^+$ organoids. (J–Q) Recombined tdTomato$^+$/Lgr5-GFP$^+$ ISCs failing to divide in DLG1$^-$ organoids. Arrowheads follow the fate of recombined ISCs. The asterisk indicates the background signal in the crypt lumen. Scale bars, 20 μm.

(R) Experimental schematic for analyzing the cell division of organoid crypt cells. Organoids grown in ENR medium for 48 h were treated with 0.25 μM 4-OHT for 24 h prior live imaging.

(S–d) Frames from time-lapse imaging of organoid crypts mosaically expressing mG. Actively dividing cells highlighted in pseudo-colors and indicated by arrowheads. Scale bars, 20 μm. (S, W, and a) Dividing cell (arrowhead) is still attached to the basal side and aligned with other cells in the crypt. (T, X, and b) Dividing cell (arrowhead) is rounded up and detached from the basal side of the crypt, undergoing cell division. (U and V) Newly divided daughter cells (arrowheads) in DLG1$^+$ crypt. (Y, Z, c, and d) Cell blebbing and fragmented cell debris in DLG1$^-$ crypt with no daughter cells post-mitosis.

(e) Quantification of cell extrusion events per crypt. n = 2–3 organoid lines per condition, mean ± SD, unpaired t test with Welch's correction.

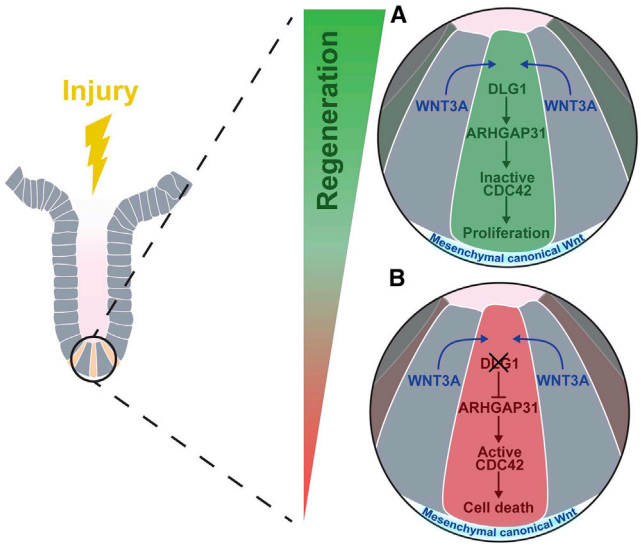

Figure 7. Model of ISC response to canonical WNT ligands via DLG1-ARHGAP31-CDC42 molecular axis

Intestinal epithelial regeneration relies on the ISC response to increased levels of Wnt signaling.

(A) DLG1 is dispensable during homeostasis when levels of Wnt signaling are low. When levels of canonical Wnt are increased in the crypt, DLG1 mediates the cellular response by regulating the expression of GTPase-activating protein *Arhgap31*, a negative regulator of CDC42 activity, and low levels of active CDC42 promote crypt regeneration.

(B) Deletion of DLG1 in ISCs and crypt cells results in decreased expression of *Arhgap31*. Due to low levels of ARHGAP31, cells accumulate active CDC42, which impairs the capacity of ISCs to undergo cell division following increased Wnt signaling and ultimately leads to cell death.

In summary, our results demonstrate that ISCs respond to fluctuating signaling pathways and reveal a link between canonical Wnt ligands and a non-canonical Wnt response, providing further insights into the niche-stem cell interaction.

Limitations of the study

Our experiments focused on ISCs, but it is possible that the WNT3A-DLG1-ARHGAP31-CDC42 molecular axis described here is not exclusive to ISCs. For example, this mechanism may also control the more rapidly cycling TA cells, which are exposed to Wnt signals coming from Paneth cells and underlying mesenchyme.

In addition, the scant number of reliable readouts of active Cdc42 and of genetic tools for manipulating its inactive and active states in mice makes it difficult to conduct a deeper dissection of intestinal Cdc42 in the non-canonical Wnt pathway. Thus, it is of particular interest and importance to generate a more robust toolkit for the study of Cdc42, including conditional alleles of the active form of Cdc42, to further explore its role in homeostasis, regeneration, and disease.

STAR★METHODS

Detailed methods are provided in the online version of this paper and include the following:

SUPPLEMENTAL INFORMATION

Supplemental information can be found online at https://doi.org/10.1016/j.stem.2022.12.008.

ACKNOWLEDGMENTS

We thank Brooks Hoehn, Evelyn Sandoval, Asoka Rathnayake, and Sergio Lopez for their technical assistance and Drs. Kara L. McKinley, Amnon Sharir, Laura Sanman, and Rachel Zwick for their helpful discussions. This work was funded by NIH R35-DE026602 and by U01DK103147 from the Intestinal Stem Cell Consortium, a collaborative research project funded by the NIDDK and the NIAID, to O.D.K. T.N. was supported by NIH R35-GM136348. D.C.-A. was supported by NIH K99-AG071933.

AUTHOR CONTRIBUTIONS

Conceptualization and design, D.C.-A., T.W., J.S., S.V., T.N., and O.D.K.; data generation, D.C.-A., T.W., E.A.R., A.G., and C.B.; data analysis and interpretation, D.C.-A., T.W., N.L.-V., S.B., M.K.E., T.N., and O.D.K.; writing – original draft, D.C.-A. and T.W.; writing – review & editing, D.C.-A., T.W., E.A.R., A.G., J.S., S.V., N.L.-V., C.B., S.B., M.K.E., T.N., and O.D.K.

DECLARATION OF INTERESTS

D.C.-A. is an employee of Genentech, Inc. and a shareholder of Roche.

Received: March 14, 2022
Revised: October 13, 2022
Accepted: December 12, 2022
Published: January 13, 2023

REFERENCES

1. Blanpain, C., and Fuchs, E. (2014). Stem cell plasticity. Plasticity of epithelial stem cells in tissue regeneration. Science *344*, 1242281. https://doi.org/10.1126/science.1242281.
2. Wells, J.M., and Watt, F.M. (2018). Diverse mechanisms for endogenous regeneration and repair in mammalian organs. Nature *557*, 322–328. https://doi.org/10.1038/s41586-018-0073-7.
3. Barker, N., van Es, J.H., Kuipers, J., Kujala, P., van den Born, M., Cozijnsen, M., Haegebarth, A., Korving, J., Begthel, H., Peters, P.J., and Clevers, H. (2007). Identification of stem cells in small intestine and colon by marker gene Lgr5. Nature *449*, 1003–1007. https://doi.org/10.1038/nature06196.
4. Barker, N., Bartfeld, S., and Clevers, H. (2010). Tissue-resident adult stem cell populations of rapidly self-renewing organs. Stem Cell *7*, 656–670. https://doi.org/10.1016/j.stem.2010.11.016.
5. Sender, R., and Milo, R. (2021). The distribution of cellular turnover in the human body. Nat. Med. *27*, 45–48. https://doi.org/10.1038/s41591-020-01182-9.
6. Sato, T., Vries, R.G., Snippert, H.J., van de Wetering, M., Barker, N., Stange, D.E., van Es, J.H., Abo, A., Kujala, P., Peters, P.J., Clevers, H., et al. (2009). Single Lgr5 stem cells build crypt-villus structures in vitro without a mesenchymal niche. Nature *459*, 262–265. https://doi.org/10.1038/nature07935.
7. Jones, D.L., and Wagers, A.J. (2008). No place like home: anatomy and function of the stem cell niche. Nat. Rev. Mol. Cell Biol. *9*, 11–21. https://doi.org/10.1038/nrm2319.
8. Scadden, D.T. (2006). The stem-cell niche as an entity of action. Nature *441*, 1075–1079. https://doi.org/10.1038/nature04957.
9. Biteau, B., Hochmuth, C.E., and Jasper, H. (2011). Maintaining tissue homeostasis: dynamic control of somatic stem cell activity. Cell Stem Cell *9*, 402–411. https://doi.org/10.1016/j.stem.2011.10.004.
10. Morrison, S.J., and Spradling, A.C. (2008). Stem cells and niches: mechanisms that promote stem cell maintenance throughout life. Cell *132*, 598–611. https://doi.org/10.1016/j.cell.2008.01.038.
11. Stzepourginski, I., Nigro, G., Jacob, J.M., Dulauroy, S., Sansonetti, P.J., Eberl, G., and Peduto, L. (2017). CD34+ mesenchymal cells are a major component of the intestinal stem cells niche at homeostasis and after injury. Proc. Natl. Acad. Sci. USA *114*, E506–E513. https://doi.org/10.1073/pnas.1620059114.
12. Yan, K.S., Janda, C.Y., Chang, J., Zheng, G.X.Y., Larkin, K.A., Luca, V.C., Chia, L.A., Mah, A.T., Han, A., Terry, J.M., et al. (2017). Non-equivalence of Wnt and R-spondin ligands during Lgr5(+) intestinal stem-cell self-renewal. Nature *545*, 238–242. https://doi.org/10.1038/nature22313.
13. Sato, T., van Es, J.H., Snippert, H.J., Stange, D.E., Vries, R.G., van den Born, M., Barker, N., Shroyer, N.F., van de Wetering, M., and Clevers, H. (2011). Paneth cells constitute the niche for Lgr5 stem cells in intestinal crypts. Nature *469*, 415–418. https://doi.org/10.1038/nature09637.
14. Clevers, H., Loh, K.M., and Nusse, R. (2014). Stem cell signaling. An integral program for tissue renewal and regeneration: Wnt signaling and stem cell control. Science *346*, 1248012. https://doi.org/10.1126/science.1248012.
15. Valenta, T., Degirmenci, B., Moor, A.E., Herr, P., Zimmerli, D., Moor, M.B., Hausmann, G., Cantù, C., Aguet, M., and Basler, K. (2016). Wnt ligands secreted by subepithelial mesenchymal cells are essential for the survival of intestinal stem cells and gut homeostasis. Cell Rep. *15*, 911–918. https://doi.org/10.1016/j.celrep.2016.03.088.
16. Shoshkes-Carmel, M., Wang, Y.J., Wangensteen, K.J., Tóth, B., Kondo, A., Massasa, E.E., Itzkovitz, S., and Kaestner, K.H. (2018). Subepithelial telocytes are an important source of Wnts that supports intestinal crypts. Nature *557*, 242–246. https://doi.org/10.1038/s41586-018-0084-4.
17. Zou, W.Y., Blutt, S.E., Zeng, X.L., Chen, M.S., Lo, Y.H., Castillo-Azofeifa, D., Klein, O.D., Shroyer, N.F., Donowitz, M., and Estes, M.K. (2018). Epithelial WNT ligands are essential drivers of intestinal stem cell activation. Cell Rep. *22*, 1003–1015. https://doi.org/10.1016/j.celrep.2017.12.093.
18. Gregorieff, A., Pinto, D., Begthel, H., Destrée, O., Kielman, M., and Clevers, H. (2005). Expression pattern of Wnt signaling components in the adult intestine. Gastroenterology *129*, 626–638. https://doi.org/10.1016/j.gastro.2005.06.007.
19. Tikhonova, A.N., Lasry, A., Austin, R., and Aifantis, I. (2020). Cell-by-cell deconstruction of stem cell niches. Cell Stem Cell *27*, 19–34. https://doi.org/10.1016/j.stem.2020.06.013.
20. Fevr, T., Robine, S., Louvard, D., and Huelsken, J. (2007). Wnt/beta-catenin is essential for intestinal homeostasis and maintenance of intestinal stem cells. Mol. Cell. Biol. *27*, 7551–7559. https://doi.org/10.1128/MCB.01034-07.
21. Kuhnert, F., Davis, C.R., Wang, H.T., Chu, P., Lee, M., Yuan, J., Nusse, R., and Kuo, C.J. (2004). Essential requirement for Wnt signaling in proliferation of adult small intestine and colon revealed by adenoviral expression of Dickkopf-1. Proc. Natl. Acad. Sci. USA *101*, 266–271. https://doi.org/10.1073/pnas.2536800100.
22. Pinto, D., Gregorieff, A., Begthel, H., and Clevers, H. (2003). Canonical Wnt signals are essential for homeostasis of the intestinal epithelium. Genes Dev. *17*, 1709–1713. https://doi.org/10.1101/gad.267103.
23. Korinek, V., Barker, N., Moerer, P., van Donselaar, E., Huls, G., Peters, P.J., and Clevers, H. (1998). Depletion of epithelial stem-cell compartments in the small intestine of mice lacking Tcf-4. Nat. Genet. *19*, 379–383.
24. Hoffman, J., Kuhnert, F., Davis, C.R., and Kuo, C.J. (2004). Wnts as essential growth factors for the adult small intestine and colon. Cell Cycle *3*, 554–557.
25. Davies, P.S., Dismuke, A.D., Powell, A.E., Carroll, K.H., and Wong, M.H. (2008). Wnt-reporter expression pattern in the mouse intestine during homeostasis. BMC Gastroenterol. *8*, 57. https://doi.org/10.1186/1471-230X-8-57.
26. Moparthi, L., and Koch, S. (2019). Wnt signaling in intestinal inflammation. Differentiation *108*, 24–32. https://doi.org/10.1016/j.diff.2019.01.002.
27. Konsavage, W.M., Jr., Jin, G., and Yochum, G.S. (2012). The Myc 3′ Wnt-responsive element regulates homeostasis and regeneration in the mouse intestinal tract. Mol. Cell. Biol. *32*, 3891–3902. https://doi.org/10.1128/MCB.00548-12.
28. Bernal, N.P., Stehr, W., Zhang, Y., Profitt, S., Erwin, C.R., and Warner, B.W. (2005). Evidence for active Wnt signaling during postresection intestinal adaptation. J. Pediatr. Surg. *40*, 1025–1029. discussion 1029. https://doi.org/10.1016/j.jpedsurg.2005.03.021.
29. Castillo-Azofeifa, D., Fazio, E.N., Nattiv, R., Good, H.J., Wald, T., Pest, M.A., de Sauvage, F.J., Klein, O.D., and Asfaha, S. (2019). Atoh1(+) secretory progenitors possess renewal capacity independent of Lgr5(+) cells during colonic regeneration. EMBO J. *38*, e99984. https://doi.org/10.15252/embj.201899984.
30. Saha, S., Aranda, E., Hayakawa, Y., Bhanja, P., Atay, S., Brodin, N.P., Li, J., Asfaha, S., Liu, L., Tailor, Y., et al. (2016). Macrophage-derived extracellular vesicle-packaged WNTs rescue intestinal stem cells and enhance survival after radiation injury. Nat. Commun. *7*, 13096. https://doi.org/10.1038/ncomms13096.
31. Voloshanenko, O., Erdmann, G., Dubash, T.D., Augustin, I., Metzig, M., Moffa, G., Hundsrucker, C., Kerr, G., Sandmann, T., Anchang, B., et al. (2013). Wnt secretion is required to maintain high levels of Wnt activity in colon cancer cells. Nat. Commun. *4*, 2610. https://doi.org/10.1038/ncomms3610.
32. Sansom, O.J., Reed, K.R., Hayes, A.J., Ireland, H., Brinkmann, H., Newton, I.P., Batlle, E., Simon-Assmann, P., Clevers, H., Nathke, I.S., et al. (2004). Loss of Apc in vivo immediately perturbs Wnt signaling, differentiation, and migration. Genes Dev. *18*, 1385–1390. https://doi.org/10.1101/gad.287404.

33. Ashton, G.H., Morton, J.P., Myant, K., Phesse, T.J., Ridgway, R.A., Marsh, V., Wilkins, J.A., Athineos, D., Muncan, V., Kemp, R., et al. (2010). Focal adhesion kinase is required for intestinal regeneration and tumorigenesis downstream of Wnt/c-Myc signaling. Dev. Cell *19*, 259–269. https://doi.org/10.1016/j.devcel.2010.07.015.

34. Shibata, H., Toyama, K., Shioya, H., Ito, M., Hirota, M., Hasegawa, S., Matsumoto, H., Takano, H., Akiyama, T., Toyoshima, K., et al. (1997). Rapid colorectal adenoma formation initiated by conditional targeting of the Apcgene. Science *278*, 120–123. https://doi.org/10.1126/science.278.5335.120.

35. Major, M.B., Camp, N.D., Berndt, J.D., Yi, X., Goldenberg, S.J., Hubbert, C., Biechele, T.L., Gingras, A.C., Zheng, N., MacCoss, M.J., et al. (2007). Wilms tumor suppressor WTX negatively regulates WNT/ß-catenin signaling. Science *316*, 1043–1046. https://doi.org/10.1126/science/1141515.

36. Parker, T.W., and Neufeld, K.L. (2020). APC controls Wnt-induced beta-catenin destruction complex recruitment in human colonocytes. Sci. Rep. *10*, 2957. https://doi.org/10.1038/s41598-020-59899-z.

37. Matsumine, A., Ogai, A., Senda, T., Okumura, N., Satoh, K., Baeg, G.H., Kawahara, T., Kobayashi, S., Okada, M., Toyoshima, K., and Akiyama, T. (1996). Binding of APC to the human homolog of the *Drosophila* discs large tumor suppressor protein. Science *272*, 1020–1023. https://doi.org/10.1126/science.272.5264.1020.

38. Yanai, H., Satoh, K., Matsumine, A., and Akiyama, T. (2000). The colorectal tumour suppressor APC is present in the NMDA-receptor-PSD-95 complex in the brain. Genes Cells *5*, 815–822. https://doi.org/10.1046/j.1365-2443.2000.00368.x.

39. Zhang, Z., Li, H., Chen, L., Lu, X., Zhang, J., Xu, P., Lin, K., and Wu, G. (2011). Molecular basis for the recognition of adenomatous polyposis coli by the Discs Large 1 protein. PLoS One *6*, e23507. https://doi.org/10.1371/journal.pone.0023507.

40. Bonello, T.T., and Peifer, M. (2019). Scribble: a master scaffold in polarity, adhesion, synaptogenesis, and proliferation. J. Cell Biol. *218*, 742–756. https://doi.org/10.1083/jcb.201810103.

41. Pearson, H.B., McGlinn, E., Phesse, T.J., Schlüter, H., Srikumar, A., Gödde, N.J., Woelwer, C.B., Ryan, A., Phillips, W.A., Ernst, M., et al. (2015). The polarity protein Scrib mediates epidermal development and exerts a tumor suppressive function during skin carcinogenesis. Mol. Cancer *14*, 169. https://doi.org/10.1186/s12943-015-0440-z.

42. Caruana, G., and Bernstein, A. (2001). Craniofacial dysmorphogenesis including cleft palate in mice with an insertional mutation in the discs large gene. Mol. Cell. Biol. *21*, 1475–1483. https://doi.org/10.1128/MCB.21.5.1475-1483.2001.

43. Naim, E., Bernstein, A., Bertram, J.F., and Caruana, G. (2005). Mutagenesis of the epithelial polarity gene, discs large 1, perturbs nephrogenesis in the developing mouse kidney. Kidney Int. *68*, 955–965. https://doi.org/10.1111/j.1523-1755.2005.00489.x.

44. Nguyen, M.M., Nguyen, M.L., Caruana, G., Bernstein, A., Lambert, P.F., and Griep, A.E. (2003). Requirement of PDZ-containing proteins for cell cycle regulation and differentiation in the mouse lens epithelium. Mol. Cell. Biol. *23*, 8970–8981. https://doi.org/10.1128/MCB.23.24.8970-8981.2003.

45. Iizuka-Kogo, A., Senda, T., Akiyama, T., Shimomura, A., Nomura, R., Hasegawa, Y., Yamamura, K., Kogo, H., Sawai, N., and Matsuzaki, T. (2015). Requirement of DLG1 for cardiovascular development and tissue elongation during cochlear, enteric, and skeletal development: possible role in convergent extension. PLoS One *10*, e0123965. https://doi.org/10.1371/journal.pone.0123965.

46. Zhang, Z., Zhang, F., Davis, A.K., Xin, M., Walz, G., Tian, W., and Zheng, Y. (2022). CDC42 controlled apical-basal polarity regulates intestinal stem cell to transit amplifying cell fate transition via YAP-EGF-mTOR signaling. Cell Rep. *38*, 110009. https://doi.org/10.1016/j.celrep.2021.110009.

47. Chen, J., Sayadian, A.C., Lowe, N., Lovegrove, H.E., and St Johnston, D. (2018). An alternative mode of epithelial polarity in the *Drosophila* midgut. PLoS Biol. *16*, e3000041. https://doi.org/10.1371/journal.pbio.3000041.

48. Etienne-Manneville, S., Manneville, J.B., Nicholls, S., Ferenczi, M.A., and Hall, A. (2005). Cdc42 and Par6-PKCzeta regulate the spatially localized association of Dlg1 and APC to control cell polarization. J. Cell Biol. *170*, 895–901. https://doi.org/10.1083/jcb.200412172.

49. Ishidate, T., Matsumine, A., Toyoshima, K., and Akiyama, T. (2000). The APC-hDLG complex negatively regulates cell cycle progression from the G0/G1 to S phase. Oncogene *19*, 365–372. https://doi.org/10.1038/sj.onc.1203309.

50. Mimori-Kiyosue, Y., Matsui, C., Sasaki, H., and Tsukita, S. (2007). Adenomatous polyposis coli (APC) protein regulates epithelial cell migration and morphogenesis via PDZ domain-based interactions with plasma membranes. Genes Cells *12*, 219–233. https://doi.org/10.1111/j.1365-2443.2007.01045.x.

51. Young, M.A., May, S., Damo, A., Yoon, Y.S., Hur, M.W., Swat, W., and Parry, L. (2019). Epigenetic regulation of Dlg1, via Kaiso, alters mitotic spindle polarity and promotes intestinal tumorigenesis. Mol. Cancer Res. *17*, 686–696. https://doi.org/10.1158/1541-7786.MCR-18-0280.

52. Caron, C., DeGeer, J., Fournier, P., Duquette, P.M., Luangrath, V., Ishii, H., Karimzadeh, F., Lamarche-Vane, N., and Royal, I. (2016). CdGAP/ARHGAP31, a Cdc42/Rac1 GTPase regulator, is critical for vascular development and VEGF-mediated angiogenesis. Sci. Rep. *6*, 27485. https://doi.org/10.1038/srep27485.

53. Kirjavainen, A., Laos, M., Anttonen, T., and Pirvola, U. (2015). The Rho GTPase Cdc42 regulates hair cell planar polarity and cellular patterning in the developing cochlea. Biol. Open *4*, 516–526. https://doi.org/10.1242/bio.20149753.

54. Stephenson, L.M., Sammut, B., Graham, D.B., Chan-Wang, J., Brim, K.L., Huett, A.S., Miletic, A.V., Kloeppel, T., Landry, A., Xavier, R., and Swat, W. (2007). DLGH1 is a negative regulator of T-lymphocyte proliferation. Mol. Cell. Biol. *27*, 7574–7581. https://doi.org/10.1128/MCB.00439-07.

55. el Marjou, F., Janssen, K.P., Chang, B.H., Li, M., Hindie, V., Chan, L., Louvard, D., Chambon, P., Metzger, D., and Robine, S. (2004). Tissue-specific and inducible Cre-mediated recombination in the gut epithelium. Genesis *39*, 186–193. https://doi.org/10.1002/gene.20042.

56. Mahoney, Z.X., Sammut, B., Xavier, R.J., Cunningham, J., Go, G., Brim, K.L., Stappenbeck, T.S., Miner, J.H., and Swat, W. (2006). Discs-large homolog 1 regulates smooth muscle orientation in the mouse ureter. Proc. Natl. Acad. Sci. USA *103*, 19872–19877. https://doi.org/10.1073/pnas.0609326103.

57. Gagnoux-Palacios, L., Awina, H., Audebert, S., Rossin, A., Mondin, M., Borgese, F., Planas-Botey, C., Mettouchi, A., Borg, J.P., and Hueber, A.O. (2018). Cell polarity and adherens junction formation inhibit epithelial Fas cell death receptor signaling. J. Cell Biol. *217*, 3839–3852. https://doi.org/10.1083/jcb.201805071.

58. Desai, R.A., Gao, L., Raghavan, S., Liu, W.F., and Chen, C.S. (2009). Cell polarity triggered by cell-cell adhesion via E-cadherin. J. Cell Sci. *122*, 905–911. https://doi.org/10.1242/jcs.028183.

59. Wang, X., Dong, B., Zhang, K., Ji, Z., Cheng, C., Zhao, H., Sheng, Y., Li, X., Fan, L., Xue, W., et al. (2018). E-cadherin bridges cell polarity and spindle orientation to ensure prostate epithelial integrity and prevent carcinogenesis in vivo. PLoS Genet. *14*, e1007609. https://doi.org/10.1371/journal.pgen.1007609.

60. Weaver, V.M., Lelièvre, S., Lakins, J.N., Chrenek, M.A., Jones, J.C., Giancotti, F., Werb, Z., and Bissell, M.J. (2002). beta4 integrin-dependent formation of polarized three-dimensional architecture confers resistance to apoptosis in normal and malignant mammary epithelium. Cancer Cell *2*, 205–216. https://doi.org/10.1016/s1535-6108(02)00125-3.

61. Myllymäki, S.M., Teräväinen, T.P., and Manninen, A. (2011). Two distinct integrin-mediated mechanisms contribute to apical lumen formation in epithelial cells. PLoS One *6*, e19453. https://doi.org/10.1371/journal.pone.0019453.

62. Casaletto, J.B., Saotome, I., Curto, M., and McClatchey, A.I. (2011). Ezrin-mediated apical integrity is required for intestinal homeostasis. Proc. Natl. Acad. Sci. USA *108*, 11924–11929. https://doi.org/10.1073/pnas.1103418108.

63. Woods, D.F., Hough, C., Peel, D., Callaini, G., and Bryant, P.J. (1996). Dlg protein is required for junction structure, cell polarity, and proliferation control in *Drosophila* epithelia. J. Cell Biol. *134*, 1469–1482. https://doi.org/10.1083/jcb.134.6.1469.

64. Valdano, M.B., Cavatorta, A.L., Morale, M.G., Marziali, F., de Souza Lino, V., Steenbergen, R.D.M., Boccardo, E., and Gardiol, D. (2016). Disc large 1 expression is altered by human papillomavirus E6/E7 proteins in organotypic cultures of human keratinocytes. J. Gen. Virol. *97*, 453–462. https://doi.org/10.1099/jgv.0.000364.

65. Iizuka-Kogo, A., Ishidao, T., Akiyama, T., and Senda, T. (2007). Abnormal development of urogenital organs in Dlgh1-deficient mice. Development *134*, 1799–1807. https://doi.org/10.1242/dev.02830.

66. Rivera, C., Yamben, I.F., Shatadal, S., Waldof, M., Robinson, M.L., and Griep, A.E. (2009). Cell-autonomous requirements for Dlg-1 for lens epithelial cell structure and fiber cell morphogenesis. Dev. Dyn. *238*, 2292–2308. https://doi.org/10.1002/dvdy.22036.

67. Humbert, P.O., Grzeschik, N.A., Brumby, A.M., Galea, R., Elsum, I., and Richardson, H.E. (2008). Control of tumourigenesis by the Scribble/Dlg/Lgl polarity module. Oncogene *27*, 6888–6907. https://doi.org/10.1038/onc.2008.341.

68. Clevers, H. (2006). Wnt/beta-catenin signaling in development and disease. Cell *127*, 469–480. https://doi.org/10.1016/j.cell.2006.10.018.

69. Xu, S., Zhou, F., Tao, J., Song, L., Ng, S.C., Wang, X., Chen, L., Yi, F., Ran, Z., Zhou, R., and Xia, B. (2014). Exome sequencing identifies DLG1 as a novel gene for potential susceptibility to Crohn's disease in a Chinese family study. PLoS One *9*, e99807. https://doi.org/10.1371/journal.pone.0099807.

70. Stoll, M., Corneliussen, B., Costello, C.M., Waetzig, G.H., Mellgard, B., Koch, W.A., Rosenstiel, P., Albrecht, M., Croucher, P.J., Seegert, D., et al. (2004). Genetic variation in DLG5 is associated with inflammatory bowel disease. Nat. Genet. *36*, 476–480. https://doi.org/10.1038/ng1345.

71. Yoshimi, K., Tanaka, T., Serikawa, T., and Kuramoto, T. (2013). Tumor suppressor APC protein is essential in mucosal repair from colonic inflammation through angiogenesis. Am. J. Pathol. *182*, 1263–1274. https://doi.org/10.1016/j.ajpath.2012.12.005.

72. McGovern, D.P., Gardet, A., Törkvist, L., Goyette, P., Essers, J., Taylor, K.D., Neale, B.M., Ong, R.T., Lagacé, C., Li, C., et al. (2010). Genome-wide association identifies multiple ulcerative colitis susceptibility loci. Nat. Genet. *42*, 332–337. https://doi.org/10.1038/ng.549.

73. Cui, H., Shu-Hong, Y., and Qiao, M. (2016). Expression of DLG1 and DLG5 in the intestinal epithelium of patients with CD. Inflamm. Bowel Dis. *22*, E43–E44. https://doi.org/10.1097/MIB.0000000000000948.

74. Zhan, T., Ambrosi, G., Wandmacher, A.M., Rauscher, B., Betge, J., Rindtorff, N., Häussler, R.S., Hinsenkamp, I., Bamberg, L., Hessling, B., et al. (2019). MEK inhibitors activate Wnt signalling and induce stem cell plasticity in colorectal cancer. Nat. Commun. *10*, 2197. https://doi.org/10.1038/s41467-019-09898-0.

75. Greenberg, H.B., and Estes, M.K. (2009). Rotaviruses: from pathogenesis to vaccination. Gastroenterology *136*, 1939–1951. https://doi.org/10.1053/j.gastro.2009.02.076.

76. Ramig, R.F. (2004). Pathogenesis of intestinal and systemic rotavirus infection. J. Virol. *78*, 10213–10220. https://doi.org/10.1128/JVI.78.19.10213-10220.2004.

77. Conner, M.E., and Ramig, R.F. (1997). Viral enteric diseases. In Viral Pathogenesis, N. Nathanson, ed. (Lippincott-Raven Publishers), pp. 713–743.

78. Mustata, R.C., Vasile, G., Fernandez-Vallone, V., Strollo, S., Lefort, A., Libert, F., Monteyne, D., Pérez-Morga, D., Vassart, G., and Garcia, M.I. (2013). Identification of Lgr5-independent spheroid-generating progenitors of the mouse fetal intestinal epithelium. Cell Rep. *5*, 421–432. https://doi.org/10.1016/j.celrep.2013.09.005.

79. Nusse, Y.M., Savage, A.K., Marangoni, P., Rosendahl-Huber, A.K.M., Landman, T.A., de Sauvage, F.J., Locksley, R.M., and Klein, O.D. (2018). Parasitic helminths induce fetal-like reversion in the intestinal stem cell niche. Nature *559*, 109–113. https://doi.org/10.1038/s41586-018-0257-1.

80. Yui, S., Azzolin, L., Maimets, M., Pedersen, M.T., Fordham, R.P., Hansen, S.L., Larsen, H.L., Guiu, J., Alves, M.R.P., Rundsten, C.F., et al. (2018). YAP/TAZ-dependent reprogramming of colonic epithelium links ECM remodeling to tissue regeneration. Cell Stem Cell *22*. 35–49.e7. https://doi.org/10.1016/j.stem.2017.11.001.

81. Merenda, A., Fenderico, N., and Maurice, M.M. (2020). Wnt signaling in 3D: recent advances in the applications of intestinal organoids. Trends Cell Biol. *30*, 60–73. https://doi.org/10.1016/j.tcb.2019.10.003.

82. Sprangers, J., Zaalberg, I.C., and Maurice, M.M. (2021). Organoid-based modeling of intestinal development, regeneration, and repair. Cell Death Differ. *28*, 95–107. https://doi.org/10.1038/s41418-020-00665-z.

83. Fordham, R.P., Yui, S., Hannan, N.R., Soendergaard, C., Madgwick, A., Schweiger, P.J., Nielsen, O.H., Vallier, L., Pedersen, R.A., Nakamura, T., et al. (2013). Transplantation of expanded fetal intestinal progenitors contributes to colon regeneration after injury. Cell Stem Cell *13*, 734–744. https://doi.org/10.1016/j.stem.2013.09.015.

84. McCarthy, N., Manieri, E., Storm, E.E., Saadatpour, A., Luoma, A.M., Kapoor, V.N., Madha, S., Gaynor, L.T., Cox, C., Keerthivasan, S., et al. (2020). Distinct mesenchymal cell populations generate the essential intestinal BMP signaling gradient. Cell Stem Cell *26*. 391–402.e5. https://doi.org/10.1016/j.stem.2020.01.008.

85. Miyoshi, H., Ajima, R., Luo, C.T., Yamaguchi, T.P., and Stappenbeck, T.S. (2012). Wnt5a potentiates TGF-β signaling to promote colonic crypt regeneration after tissue injury. Science *338*, 108–113. https://doi.org/10.1126/science.1223821.

86. Lamarche-Vane, N., and Hall, A. (1998). CdGAP, a novel proline-rich GTPase-activating protein for Cdc42 and Rac. J. Biol. Chem. *273*, 29172–29177. https://doi.org/10.1074/jbc.273.44.29172.

87. Tcherkezian, J., Triki, I., Stenne, R., Danek, E.I., and Lamarche-Vane, N. (2006). The human orthologue of CdGAP is a phosphoprotein and a GTPase-activating protein for Cdc42 and Rac1 but not RhoA. Biol. Cell *98*, 445–456. https://doi.org/10.1042/BC20050101.

88. LaLonde, D.P., Grubinger, M., Lamarche-Vane, N., and Turner, C.E. (2006). CdGAP associates with actopaxin to regulate integrin-dependent changes in cell morphology and motility. Curr. Biol. *16*, 1375–1385. https://doi.org/10.1016/j.cub.2006.05.057.

89. Mehra, C., Chung, J.H., He, Y., Lara-Márquez, M., Goyette, M.A., Boufaied, N., Barrès, V., Ouellet, V., Guérard, K.P., Delliaux, C., et al. (2021). CdGAP promotes prostate cancer metastasis by regulating epithelial-to-mesenchymal transition, cell cycle progression, and apoptosis. Commun. Biol. *4*, 1042. https://doi.org/10.1038/s42003-021-02520-4.

90. Thorne, C.A., Chen, I.W., Sanman, L.E., Cobb, M.H., Wu, L.F., and Altschuler, S.J. (2018). Enteroid monolayers reveal an autonomous WNT and BMP circuit controlling intestinal epithelial growth and organization. Dev. Cell *44*. 624–633.e4. https://doi.org/10.1016/j.devcel.2018.01.024.

91. Lamarche, N., Tapon, N., Stowers, L., Burbelo, P.D., Aspenström, P., Bridges, T., Chant, J., and Hall, A. (1996). Rac and Cdc42 induce actin polymerization and G1 cell cycle progression independently of p65PAK and the JNK/SAPK MAP kinase cascade. Cell *87*, 519–529. https://doi.org/10.1016/s0092-8674(00)81371-9.

92. Ueyama, T. (2019). Rho-family small GTPases: from highly polarized sensory neurons to cancer cells. Cells *8*, 92. https://doi.org/10.3390/cells8020092.

93. Melendez, J., Liu, M., Sampson, L., Akunuru, S., Han, X., Vallance, J., Witte, D., Shroyer, N., and Zheng, Y. (2013). Cdc42 coordinates proliferation, polarity, migration, and differentiation of small intestinal epithelial

cells in mice. Gastroenterology *145*, 808–819. https://doi.org/10.1053/j.gastro.2013.06.021.

94. McKinley, K.L., Stuurman, N., Royer, L.A., Schartner, C., Castillo-Azofeifa, D., Delling, M., Klein, O.D., and Vale, R.D. (2018). Cellular aspect ratio and cell division mechanics underlie the patterning of cell progeny in diverse mammalian epithelia. eLife *7*, e36739. https://doi.org/10.7554/eLife.36739.
95. Lane, S.W., Williams, D.A., and Watt, F.M. (2014). Modulating the stem cell niche for tissue regeneration. Nat. Biotechnol. *32*, 795–803. https://doi.org/10.1038/nbt.2978.
96. Gehart, H., and Clevers, H. (2019). Tales from the crypt: new insights into intestinal stem cells. Nat. Rev. Gastroenterol. Hepatol. *16*, 19–34. https://doi.org/10.1038/s41575-018-0081-y.
97. Tan, D.W., and Barker, N. (2014). Intestinal stem cells and their defining niche. Curr. Top. Dev. Biol. *107*, 77–107. https://doi.org/10.1016/B978-0-12-416022-4.00003-2.
98. Nusse, R., and Clevers, H. (2017). Wnt/beta-catenin signaling, disease, and emerging therapeutic modalities. Cell *169*, 985–999. https://doi.org/10.1016/j.cell.2017.05.016.
99. Acebron, S.P., and Niehrs, C. (2016). Beta-catenin-independent roles of Wnt/LRP6 signaling. Trends Cell Biol. *26*, 956–967. https://doi.org/10.1016/j.tcb.2016.07.009.
100. Chae, W.J., and Bothwell, A.L.M. (2018). Canonical and non-canonical Wnt signaling in immune cells. Trends Immunol. *39*, 830–847. https://doi.org/10.1016/j.it.2018.08.006.
101. Humphries, A.C., and Mlodzik, M. (2018). From instruction to output: Wnt/PCP signaling in development and cancer. Curr. Opin. Cell Biol. *51*, 110–116. https://doi.org/10.1016/j.ceb.2017.12.005.
102. VanderVorst, K., Dreyer, C.A., Konopelski, S.E., Lee, H., Ho, H.H., and Carraway, K.L., 3rd (2019). Wnt/PCP signaling contribution to carcinoma collective cell migration and metastasis. Cancer Res. *79*, 1719–1729. https://doi.org/10.1158/0008-5472.CAN-18-2757.
103. Pinzón-Daza, M.L., Salaroglio, I.C., Kopecka, J., Garzòn, R., Couraud, P.O., Ghigo, D., and Riganti, C. (2014). The cross-talk between canonical and non-canonical Wnt-dependent pathways regulates P-glycoprotein expression in human blood-brain barrier cells. J. Cereb. Blood Flow Metab. *34*, 1258–1269. https://doi.org/10.1038/jcbfm.2014.100.
104. Glinka, A., Dolde, C., Kirsch, N., Huang, Y.L., Kazanskaya, O., Ingelfinger, D., Boutros, M., Cruciat, C.M., and Niehrs, C. (2011). LGR4 and LGR5 are R-spondin receptors mediating Wnt/beta-catenin and Wnt/PCP signalling. EMBO Rep. *12*, 1055–1061. https://doi.org/10.1038/embor.2011.175.
105. Mentink, R.A., Rella, L., Radaszkiewicz, T.W., Gybel, T., Betist, M.C., Bryja, V., and Korswagen, H.C. (2018). The planar cell polarity protein VANG-1/Vangl negatively regulates Wnt/beta-catenin signaling through a Dvl dependent mechanism. PLoS Genet. *14*, e1007840. https://doi.org/10.1371/journal.pgen.1007840.
106. Rella, L., Fernandes Póvoa, E.E., Mars, J., Ebbing, A.L.P., Schoppink, L., Betist, M.C., and Korswagen, H.C. (2021). A switch from noncanonical to canonical Wnt signaling stops neuroblast migration through a Slt-Robo and RGA-9b/ARHGAP-dependent mechanism. Proc. Natl. Acad. Sci. USA *118*. e2013239118. https://doi.org/10.1073/pnas.2013239118.
107. Bastías-Candia, S., Martínez, M., Zolezzi, J.M., and Inestrosa, N.C. (2019). Wnt signaling upregulates Teneurin-3 expression via canonical and non-canonical Wnt pathway crosstalk. Front. Neurosci. *13*, 505. https://doi.org/10.3389/fnins.2019.00505.
108. Qiu, W., Chen, L., and Kassem, M. (2011). Activation of non-canonical Wnt/JNK pathway by Wnt3a is associated with differentiation fate determination of human bone marrow stromal (mesenchymal) stem cells. Biochem. Biophys. Res. Commun. *413*, 98–104. https://doi.org/10.1016/j.bbrc.2011.08.061.
109. Flores-Hernández, E., Velázquez, D.M., Castañeda-Patlán, M.C., Fuentes-García, G., Fonseca-Camarillo, G., Yamamoto-Furusho, J.K., Romero-Avila, M.T., García-Sáinz, J.A., and Robles-Flores, M. (2020). Canonical and non-canonical Wnt signaling are simultaneously activated by Wnts in colon cancer cells. Cell. Signal. *72*, 109636. https://doi.org/10.1016/j.cellsig.2020.109636.
110. Nalesso, G., Sherwood, J., Bertrand, J., Pap, T., Ramachandran, M., De Bari, C., Pitzalis, C., and Dell'accio, F. (2011). WNT-3A modulates articular chondrocyte phenotype by activating both canonical and noncanonical pathways. J. Cell Biol. *193*, 551–564. https://doi.org/10.1083/jcb.201011051.
111. Almeida, M., Han, L., Bellido, T., Manolagas, S.C., and Kousteni, S. (2005). Wnt proteins prevent apoptosis of both uncommitted osteoblast progenitors and differentiated osteoblasts by beta-catenin-dependent and -independent signaling cascades involving Src/ERK and phosphatidylinositol 3-kinase/AKT. J. Biol. Chem. *280*, 41342–41351. https://doi.org/10.1074/jbc.M502168200.
112. Humbert, P.O., Dow, L.E., and Russell, S.M. (2006). The Scribble and Par complexes in polarity and migration: friends or foes? Trends Cell Biol. *16*, 622–630. https://doi.org/10.1016/j.tcb.2006.10.005.
113. Hu, D.J., Yun, J., Elstrott, J., and Jasper, H. (2021). Non-canonical Wnt signaling promotes directed migration of intestinal stem cells to sites of injury. Nat. Commun. *12*, 7150. https://doi.org/10.1038/s41467-021-27384-4.
114. Nalapareddy, K., Hassan, A., Sampson, L.L., Zheng, Y., and Geiger, H. (2021). Suppression of elevated Cdc42 activity promotes the regenerative potential of aged intestinal stem cells. iScience *24*, 102362. https://doi.org/10.1016/j.isci.2021.102362.
115. Dwivedi, V.K., Pardo-Pastor, C., Droste, R., Kong, J.N., Tucker, N., Denning, D.P., Rosenblatt, J., and Horvitz, H.R. (2021). Replication stress promotes cell elimination by extrusion. Nature *593*, 591–596. https://doi.org/10.1038/s41586-021-03526-y.
116. Li, Y., Junge, J.A., Arnesano, C., Gross, G.G., Miner, J.H., Moats, R., Roberts, R.W., Arnold, D.B., and Fraser, S.E. (2018). Discs large 1 controls daughter-cell polarity after cytokinesis in vertebrate morphogenesis. Proc. Natl. Acad. Sci. USA *115*, E10859–E10868. https://doi.org/10.1073/pnas.1713959115.
117. Nobes, C.D., and Hall, A. (1995). Rho, rac, and cdc42 GTPases regulate the assembly of multimolecular focal complexes associated with actin stress fibers, lamellipodia, and filopodia. Cell *81*, 53–62. https://doi.org/10.1016/0092-8674(95)90370-4.
118. Ridley, A.J., and Hall, A. (1992). The small GTP-binding protein rho regulates the assembly of focal adhesions and actin stress fibers in response to growth factors. Cell *70*, 389–399. https://doi.org/10.1016/0092-8674(92)90163-7.
119. Symons, M. (1996). Rho family GTPases: the cytoskeleton and beyond. Trends Biochem. Sci. *21*, 178–181.
120. Zhou, X., Florian, M.C., Arumugam, P., Chen, X., Cancelas, J.A., Lang, R., Malik, P., Geiger, H., and Zheng, Y. (2013). RhoA GTPase controls cytokinesis and programmed necrosis of hematopoietic progenitors. J. Exp. Med. *210*, 2371–2385. https://doi.org/10.1084/jem.20122348.
121. Dobin, A., Davis, C.A., Schlesinger, F., Drenkow, J., Zaleski, C., Jha, S., Batut, P., Chaisson, M., and Gingeras, T.R. (2013). STAR: ultrafast universal RNA-seq aligner. Bioinformatics *29*, 15–21. https://doi.org/10.1093/bioinformatics/bts635.
122. Love, M.I., Huber, W., and Anders, S. (2014). Moderated estimation of fold change and dispersion for RNA-seq data with DESeq2. Genome Biol. *15*, 550. https://doi.org/10.1186/s13059-014-0550-8.
123. Zhou, W., Zhang, L., Guoxiang, X., Mojsilovic-Petrovic, J., Takamaya, K., Sattler, R., Huganir, R., and Kalb, R. (2008). GluR1 controls dendrite growth through its binding partner, SAP97. J. Neurosci. *28*, 10220–10233. https://doi.org/10.1523/JNEUROSCI.3434-08.2008.
124. Madisen, L., Zwingman, T.A., Sunkin, S.M., Oh, S.W., Zariwala, H.A., Gu, H., Ng, L.L., Palmiter, R.D., Hawrylycz, M.J., Jones, A.R., et al. (2010). A robust and high-throughput Cre reporting and characterization system for the whole mouse brain. Nat. Neurosci. *13*, 133–140. https://doi.org/10.1038/nn.2467.

125. Muzumdar, M.D., Tasic, B., Miyamichi, K., Li, L., and Luo, L. (2007). A global double-fluorescent Cre reporter mouse. Genesis *45*, 593–605. https://doi.org/10.1002/dvg.20335.

126. Hamilton, T.G., Klinghoffer, R.A., Corrin, P.D., and Soriano, P. (2003). Evolutionary divergence of platelet-derived growth factor alpha receptor signaling mechanisms. Mol. Cell. Biol. *23*, 4013–4025. https://doi.org/10.1128/MCB.23.11.4013-4025.2003.

127. O'Neal, C.M., Crawford, S.E., Estes, M.K., and Conner, M.E. (1997). Rotavirus virus-like particles administered mucosally induce protective immunity. J. Virol. *71*, 8707–8717. https://doi.org/10.1128/JVI.71.11.8707-8717.1997.

128. Schindelin, J., Arganda-Carreras, I., Frise, E., Kaynig, V., Longair, M., Pietzsch, T., Preibisch, S., Rueden, C., Saalfeld, S., Schmid, B., et al. (2012). Fiji: an open-source platform for biological-image analysis. Nat. Methods *9*, 676–682. https://doi.org/10.1038/nmeth.2019.

129. Kabiri, Z., Greicius, G., Madan, B., Biechele, S., Zhong, Z., Zaribafzadeh, H., Edison, A., Aliyev, J., Wu, Y., Bunte, R., et al. (2014). Stroma provides an intestinal stem cell niche in the absence of epithelial Wnts. Development *141*, 2206–2215. https://doi.org/10.1242/dev.104976.

130. Sanman, L.E., Chen, I.W., Bieber, J.M., Steri, V., Trentesaux, C., Hann, B., Klein, O.D., Wu, L.F., and Altschuler, S.J. (2021). Transit-amplifying cells coordinate changes in intestinal epithelial cell-type composition. Dev. Cell *56*. 356–365.e9. https://doi.org/10.1016/j.devcel.2020.12.020.

131. Sanman, L.E., Chen, I.W., Bieber, J.M., Thorne, C.A., Wu, L.F., and Altschuler, S.J. (2020). Generation and quantitative imaging of enteroid monolayers. Methods Mol. Biol. *2171*, 99–113. https://doi.org/10.1007/978-1-0716-0747-3_6.

STAR★METHODS

KEY RESOURCES TABLE

REAGENT or RESOURCE	SOURCE	IDENTIFIER
Antibodies		
Rat monoclonal anti-CD45, clone 30-F11	Biolegend	Cat#: 103133 RRID: AB_10899570
Rat monoclonal anti-EpCAM, clone G8.8	Biolegend	Cat#: 118211 RRID: AB_1134104
Rat monoclonal anti-CD44, clone IM7	Biolegend	Cat#: 103029 RRID: AB_830786
Mouse anti-Dlg1, Clone 12/Dlg	BD Biosciences	Cat#: 610874 RRID: AB_398192
Mouse monoclonal anti-BrdU	Novus Biologicals	Cat#: NB500-439 RRID:AB_10000514
Rabbit monoclonal anti-E-cadherin	Cell Signaling Technology	Cat#: 3195S RRID:AB_2291471
Rat monoclonal anti-β4-integrin	Abcam	Cat#: ab25254 RRID:AB_2129042
Mouse monoclonal anti-Ezrin	Invitrogen	Cat#: MA5-13862
Rabbit monoclonal anti-RFP	Rockland	Cat#: 200-301-379 RRID:AB_2611063
Rabbit polyclonal anti-cleaved caspase-3	Cell Signaling	Cat#: 9661 RRID:AB_2341188
Rabbit polyclonal anti-Mucin2	Novus Biologicals	Cat#: NBP1- 31231 RRID: AB_10003763
Rabbit polyclonal anti-Chromogranin A	Abcam	Cat#: ab45179 RRID:AB_300798
Rabbit polyclonal anti-DCAMKL1	Abcam	Cat#: ab31704 RRID:AB_873537
Rabbit polyclonal anti-Lysozyme	Dako	Cat#: A0099 RRID:AB_2341230
Bacterial and virus strains		
Rotavirus strain EC_{WT} (P[17], G3)	Mary Estes	N/A
Chemicals, peptides, and recombinant proteins		
EdU: 5-ethynyl-2'-deoxyuridine	ThermoFisher	Cat#: C10637
BrdU: 5-Bromo-2'-deoxyuridine	Sigma-Aldrich	Cat#: B5002
Trametinib	ApexBio	Cat#: A3018
Tamoxifen	Sigma-Aldrich	Cat#: T5648
4-hydroxytamoxifen	Sigma-Aldrich	Cat#: H7904
TrypIE	Gibco	Cat#: 12604039
Matrigel	Corning	Cat#: 356231
WNT3A	PeproTech	Cat#: 315-20-10ug
WNT5A	R&D Systems	Cat#: 645-WN
Nicotine amide	Sigma-Aldrich	Cat#: 72340
Collagenase/Dispase	Roche	Cat#: 10269638001
293T-HA-RSPO1-Fc cells	Trevigen	Cat#: 3710-001-01
L-WNT3A cells	ATCC	Cat#: CRL-2647
Critical commercial assays		
Alkaline Phosphatase Red Substrate Kit	Vector Laboratories	Cat#: SK-5100
Click-iT™ Plus EdU Cell Proliferation Kit for Imaging	Thermo Fisher	Cat#: C10637
CellEvent™ Caspase-3/7 Green ReadyProbes™ Reagent	Thermo Fisher	Cat#: R37111

(*Continued on next page*)

Continued

REAGENT or RESOURCE	SOURCE	IDENTIFIER
RNAscope® 2.5 High Definition (HD) – Red Assay	Advanced Cell Diagnostics	Cat#: 322350
G-LISA activation assay kit for Cdc42	Cytoskeleton	Cat#: BK127
G-LISA activation assay kit for Rac1	Cytoskeleton	Cat#: BK128
polyA Dynabeads mRNA direct Kit	Invitrogen	Cat#: 61012
SmartSeq DNA library preparation Kits	Takarabio	Cat#: 634471
NexteraXT DNA library preparation Kits	Illumina	Cat#: FC-131-1024
RNeasy Mini Kit	Qiagen	Cat#: 74104
High-capacity cDNA Reverse Transcription Kit	Applied Biosystems	Cat#: 4368814
iTaq Universal SYBR Green Supermix	Bio Rad	Cat#: 1725121
Animal-free blocker	Vector Laboratories	Cat#: SP-5030
ProLong Gold Antifade	Thermo Fisher	Cat#: P36930
Deposited data		
Gene Expression Omnibus	This paper	GSE198573
Experimental models: Organisms/strains		
Mouse: *Dlg1*^{min}	Todd Nystul	Rivera et al.[66]
Mouse: *Arhgap31*^{flox}	Nathalie LaMarche Vane	Caron et al.[52]
Mouse: *Dlg1*^{flox}: B6;129-*Dlg1*^{tm1Rlh}/J	JAX	Strain #:013097 RRID:IMSR_JAX:013097
Mouse: *Lgr5*$^{GFP\text{-}CreERT2}$: B6.129P2-*Lgr5*$^{tm1(cre/ERT2)Cle}$/J	JAX	Strain #:008875 RRID:IMSR_JAX:008875
Mouse: *Villin*^{CreERT}: B6.Cg-Tg(Vil1-cre/ERT2)23Syr/J	JAX	Strain #:020282 RRID:IMSR_JAX:020282
Mouse: *ROSA26*^{tdTomato}: B6.Cg-Gt(ROSA)26Sor$^{tm14(CAG\text{-}tdTomato)Hze}$/J	JAX	Strain #:007914 RRID:IMSR_JAX:007914
Mouse: *ROSA26*^{mTmG}: B6.129(Cg)-Gt(ROSA)26Sor$^{tm4(ACTB\text{-}tdTomato,\text{-}EGFP)Luo}$/J	JAX	Strain #:007676 RRID:IMSR_JAX:007676
Mouse: *Pdgfrα*$^{H2B\text{-}eGFP}$B6.129S4-Pdgfra$^{tm11(EGFP)Sor}$/J	JAX	Strain #:007669 RRID:IMSR_JAX:007669
Oligonucleotides		
RNAscope® probe Mm-Arhgap31	Advanced Cell Diagnostics	Cat#: 569971
Oligonucleotides	Table S1	N/A
Software and algorithms		
Fiji v2.1.0/1.53c	Open source	https://imagej.net/software/fiji
GraphPad Prism9	GraphPad Software	https://www.graphpad.com
Adobe Illustrator v25.4	Adobe	https://www.adobe.com
Adobe Photoshop	Adobe	https://www.adobe.com
QuantStudio Real-time PCR software v1.3	Applied Biosystems	https://www.thermofisher.com
LasX v3.4.2	Leica	https://www.leica-microsystems.com
ZEN Blue v2.5	Zeiss	https://www.zeiss.com
STAR 2.4.2a	Dobin et al.[121]	https://code.google.com/archive/p/rna-star/
DESeq2 v1.16.1	Love et al.[122]	https://bioconductor.org/packages/release/bioc/html/DESeq2.html
BD FACS Diva v.8.0.1	BD Biosciences	https://www.bdbiosciences.com/
FlowJo v10.8	Tree Star	https://www.flowjo.com

RESOURCE AVAILABILITY

Lead contact

Further information and requests for reagents may be directed to, and will be fulfilled by, the lead contact, Ophir Klein (ophir.klein@ucsf.edu).

Materials availability
This study did not generate new unique reagents.

Data and code availability
Bulk RNA-seq data have been deposited at GEO and are publicly available as of the date of publication. Accession numbers are listed in the key resources table. Microscopy data reported in this paper will be shared by the lead contact upon request. This paper does not report original code. Any additional information required to reanalyze the data reported in this paper is available from the lead contact upon request.

EXPERIMENTAL MODEL AND SUBJECT DETAILS

Animals
All experimental procedures involving mice were done in accordance with approved protocols by the Institutional Animal Care and Use Committee (IACUC) and Laboratory Animal Resource Center (LARC) at University of California San Francisco, and the mice were handled in accordance with the principles and procedures of the Guide for the Care and Use of Laboratory Animals under the approved protocol AN180876. All mouse strains were maintained on a predominantly C57BL/6 background. Animals were housed under pathogen-free conditions in 12-hour light/dark cycles at 23 ± 1°C and humidity 55 ± 15%. Food and water were provided ad libitum. Animals were weaned 21 to 28 days after birth and handled and euthanized according to procedures approved by LARC of the University of California San Francisco. Mice were at least 8 weeks old at the time of experiments and cell isolations. Mice of the both sexes were used in all experiments, and they were either randomly assigned to the experimental groups or used with littermate controls. The *Dlg1*^{min} (i.e. *Dlg1*$^{\Delta}$)[66] and *Arhgap31*^{flox}[52] alleles were previously described. Mice harboring *Dlg1*^{flox} (Jax: 013097[123]), *Lgr5*$^{GFP\text{-}CreERT2}$ (Jax 008875[3]), *Villin*^{CreERT2} (Jax: 020282[55]), *ROSA26*^{tdTomato} (Jax 007905[124]), *ROSA26*^{mTmG} (Jax: 007676[125]), and *Pdgfr*$\alpha^{H2B\text{-}eGFP}$ (JAX: 007669[126]) alleles were purchased from The Jackson Laboratory.

METHOD DETAILS

Animal treatments
Mice were given an intraperitoneal injection of 1 mg/25 g body weight of 5-ethynyl-2'-deoxyuridine (EdU; ThermoFisher, C10637) and then analyzed at various timepoints after treatment (exact chase timepoints are provided in the main text). Mice received intraperitoneal injection of 1 mg/25 g body weight of 5-Bromo-2'-deoxyuridine (BrdU, Sigma-Aldrich, B5002-250MG) 24 hours before analysis. Mice received two intraperitoneal injections of trametinib at a dose of 2 mg/kg of body weight and intestinal tissue was analyzed 24 hours after the second administration. Trametinib was dissolved in sterile DMSO at 6.15 mg/ml and diluted in sterile 1:1 mixture PBS:DMSO to final concentration 500 μg/ml prior administration. Mice were given an intraperitoneal injection of 2.5 mg/25 g body weight of tamoxifen (Sigma-Aldrich, T5648-5G) dissolved in corn oil (Sigma-Aldrich, C8267) at concentration 25 mg/ml. Rotavirus strain EC_{WT} (P[17], G3) was prepared and administered by oral gavage as described previously.[127] All animals were housed in a physically separated BSL-2 animal facility. A 1×10^5 50% infectious dose (ID50) was used to obtain adequate infection.[127] To monitor rotavirus infection, fecal samples were collected and fecal ELISA was used as described previously.[127] Mice were sacrificed 4 days following infection at the peak of viral shedding.

Antibodies
For flow cytometry of intestinal epithelium, organoids, and PDGFRα^{lo} cells, the following antibodies were used: rat anti-CD45 (BioLegend, 30-F11; 1:100), rat anti-EpCAM (BioLegend, G8.8; 1:200), rat anti-CD44 (BioLegend, IM7; 1:100). Nuclei were counterstained with DAPI (stock concentration 5 mg/ml, Sigma-Aldrich, D9542; 1:1,000 or 10,000).

For immunofluorescence staining of sections and organoids, the following antibodies were used: mouse anti-Dlg1 (BD Biosciences, 610874; 1:200), anti-BrdU (Novus Biologicals, NB500-439; 1:100), rabbit anti-E-cadherin (Cell Signaling Technology, 3195S; 1:200), rat anti-β4-integrin (Abcam, ab25254; 1:200), mouse anti-Ezrin (Invitrogen, MA5-13862; 1:200), rabbit anti-RFP (Rockland, 200-301-379; 1:100), rabbit anti-cleaved caspase-3 (Cell Signaling, 9661; 1:200), rabbit anti-Mucin2 (Novus Biologicals, NBP1- 31231; 1:100), rabbit anti-Chromogranin A (Abcam, ab45179; 1:100), rabbit anti-DCAMKL1 (Abcam, ab31704; 1:100), rabbit anti-Lysozyme (Dako, A0099; 1:500), Alkaline Phosphatase Red Substrate Kit (Vector Laboratories, SK-5100), rabbit anti-Histone H4K16ac (Active Motif, 39068; 1:100). EdU was detected using Click-iT™ Plus EdU Cell Proliferation Kit for Imaging, Alexa Fluor™ 488 dye (ThermoFisher, C10637). Caspase-3/7 was detected using CellEvent™ Caspase-3/7 Green ReadyProbes™ Reagent (ThermoFisher, R37111). Nuclei were counterstained with DAPI (1:10,000).

Tissue preparation for immunofluorescence staining and RNAscope
For immunofluorescence staining, harvested intestinal tissue was perfusion fixed. For perfusion fixation, animals were anesthetized by intraperitoneal injection of 250 mg/kg of body weight avertin (2,2,2-tribromoethanol) and transcardially perfused with 4% paraformaldehyde (PFA) in 100 mM PBS. Dissected tissues were post-fixed in 4% PFA for 4 hours at 4°C and cryoprotected in 30% sucrose in 1× PBS overnight at 4°C. Tissue was embedded in OCT compound (Sakura, 4583), frozen, and stored at -80°C. For paraffin-embedded tissues, we post-fixed tissues with 4% PFA in 100 mM PBS for 24 hours at 4°C, followed by paraffin processing,

using a standard protocol. For RNAscope *in situ* analysis, freshly isolated intestinal tissue was immersed into 4% PFA for 24 hours at room temperature, followed by standard dehydration and paraffin embedding protocol.

Immunofluorescence staining of intestinal tissue

Immunofluorescence was performed on 7 μm cryosections or paraffin sections. Cryosections were washed with PBS, blocked with 0.3% Triton X-100 in PBS supplemented with 5% normal goat serum. Paraffin sections were rehydrated, and antigen retrieval was performed by sub-boiling slides in a pressure cooker for 30 min in a citrate buffer (pH 6.2) containing 10 mM citric acid, 2 mM EDTA and 0.05% Tween-20. For BrdU immunostaining, samples were additionally washed with 2 N HCl for 30 min. Paraffin sections were blocked in 1× animal-free blocker (Vector Laboratories, SP-5030) supplemented with 2.5% heat-inactivated goat serum, 0.02% SDS and 0.1% Triton X-100. All of the antibodies were diluted in the same blocking solution without serum and sections were incubated with primary antibodies at 4°C for 12 to 16 hours. Appropriate secondary antibodies from Thermo Fisher Scientific were used at 1:1,000 dilution. Nuclei were counterstained with DAPI. Cryosections and paraffin sections were coverslipped with ProLong Gold Antifade (Thermo Fisher Scientific, P36930).

Quantification of *Arhgap31* transcripts using RNAscope

RNA *in situ* hybridization for *Arhgap31* expression was performed on 7 μm paraffin sections using RNAscope® 2.5 High Definition (HD) – Red Assay (Advanced Cell Diagnostics, 322350). Manufacturer's protocol was followed with 15 min of target retrieval and 30 min of protease digestion, using the RNAscope® probe Mm-Arhgap31 (Advanced Cell Diagnostics, 569971). Quantification of *Arhgap31* mRNA transcripts was performed using the open-source platform Fiji[128] and the analysis guidelines from Advanced Cell Diagnostics. Area of single probes was measured and used to determine total probe count within probe clusters. Total probe clusters containing at least 10 probes were quantified and normalized to crypt area.

Organoid culture media

Complete organoid 1× ENR medium was prepared from 1× Advanced DMEM/F12, 10 mM HEPES, 2 mM Glutamax, 0.11 mg/ml Penicillin-Streptomycin antibiotics, 1 mM N-Acetylcysteine, 50 ng/ml hEGF, 100 ng/ml Noggin, 2% B-27 Supplement (Thermo Fisher Scientific, 17504044), 1% N-2 supplement (Thermo Fisher Scientific, 17502048) and 5% R-Spondin1 conditioned medium (RSPO1 CM). RSPO1 CM was prepared by harvesting conditioned medium from cultured 293T-HA-RSPO1-Fc cells (Trevigen, 3710-001-01) as described (R&D Systems Protocol; https://resources.rndsystems.com/images/site/dw_r-spondinmediumprotocol_34749-web.pdf?v=1). Aliquots of 10 ml were stored at -80°C and were thawed prior mixing the ENR medium. WNT3A conditioned medium (WNT3A CM) was generated by harvesting conditioned medium from cultured L-WNT3A cells (ATCC CRL-2647) at 1× dilution in Advanced DMEM/F12 (ThermoFisher, #11320-033) and supplemented with 10 mM HEPES (UCSF Media Production Core, #CCFGL002), 0.11 mg/ml Penicillin-Streptomycin antibiotics (UCSF Media Production Core, #CCFGK004), 2 mM Glutamax (ThermoFisher, #35050-079), 1 mM N-Acetylcysteine (Sigma, #SKU-A7250-10G) and heat inactivated 10% FBS. Aliquots of 1 ml were stored at -80°C and were thawed just prior preparing complete organoid media containing WNT3A CM. Conditioned medium from PDGFRα^{lo} cells (PDGFRα^{lo} CM) was prepared by digesting small intestinal tissue from *Pdgfrα*$^{H2B\text{-}eGFP}$ mouse for 3 h in 6 ml of serum-free DMEM containing 1% Glutamax, 1% Penicillin-Streptomycin and 2 mg/ml of Collagenase/Dispase (Roche, 10269638001) as described previously,[129] followed by FACS sorting intestinal PDGFRα^{lo} cells (DAPI^{-}/EpCAM^{-}/CD44^{-}/CD45^{-}/PDGFRα$^{H2B\text{-}GFP\text{-}lo+}$) as described previously.[84] 100,000 sorted cells were plated into 1 well of 24-well plate, and grown in 500 μl of 1× Advanced DMEM/F12, 10 mM HEPES, 2 mM Glutamax, 0.11 mg/ml Penicillin-Streptomycin antibiotics, 1 mM N-Acetylcysteine, 20% FBS, 50 ng/ml hEGF, 2% B-27 Supplement, 1% N-2 supplement. Conditioned medium was collected every 2-3 days for up to 2 passages, combined together and aliquots of 0.5 ml were stored at -80°C and were thawed prior use.

Complete organoid media containing WNT3A CM or PDGFRα^{lo} CM was prepared from 2× ENR supplemented with 50% WNT3A CM or PDGFRα^{lo} CM, and 10 mM Nicotine amide (Sigma-Aldrich, 72340). Complete organoid media containing recombinant WNT3A or WNT5A was prepared from 1× ENR supplemented with 200 ng/ml recombinant murine WNT3A (PeproTech, 315-20-10ug) or 500 ng/ml recombinant human/mouse WNT5A (R&D Systems; 645-WN), and 10 mM Nicotine amide.

Establishment of intestinal organoids from primary epithelial tissue

Organoid cultures were established from primary tissue as previously described.[130,131] Briefly, 8- to 16-week old mice were sacrificed and dissected to harvest the small intestine. Tissue was placed in 15 ml of cold 1× PBS supplemented with 0.11 mg/ml Penicillin-Streptomycin antibiotics, 2 mM DTT, 1 mM EDTA, and 10 μM Y-27632, and incubated on ice for 15 minutes. Intestines were then moved to a tube with 20 ml cold PBS with 2 mM DTT, 3 mM EDTA, 10 μM Y-27632 and incubated for additional 60 minutes followed by vigorous shaking for one minute to release crypts into solution. Crypts were separated from villi material by filtering the solution using 70 μm cell strainers, followed by 2 washes with Advanced DMEM/F12 supplemented with 10 mM HEPES, 0.11 mg/ml Penicillin-Streptomycin antibiotics, and 1 mM N-Acetylcysteine. Finally, crypts were resuspended in Matrigel (Corning, 356231) plated on 24-well culture plates and overlaid with 1× ENR medium to initiate organoid cultures (defining passage P0). Organoids were grown at 37°C in 5% CO_2 incubator, growth medium was changed at D5 and organoids were passaged at D7.

Mechanical passaging and enzymatic dissociation of intestinal organoids, and treatment

Mechanical passaging of organoids was done according to the protocols described previously.[6] Briefly, at day 7 following plating, Matrigel droplets containing organoids were disrupted with P1000 pipette, transferred to 15 ml conical tube and washed twice with 1× DMEM/F12 medium. Washed crypts were plated at a ratio 1:4 into a new Matrigel droplet and plated into plastic 24-well plates or into 12-well glass bottom plate for live-imaging.

For plating the organoids into 2D monolayer, 24-well plastic plate was first coated with 2.5% Matrigel in 1× DMEM/F12 medium. Enzymatic dissociation followed the same protocol as mechanical passaging. However, washed crypts were treated with TryplE (Gibco, 12604039) for 7 minutes at 37°C, followed by a wash with 1× ENR medium. Enzymatically dissociated organoids were resuspended and plated in the complete organoid media containing WNT3A conditioned medium. To culture 2D monolayers in complete ENR medium, organoids were only mechanically passaged and plated.

To delete *Dlg1* and *Arhgap31 in vitro*, crypts, organoids, or 2D monolayers were incubated in the presence of 1 μM 4-hydroxytamoxifen (4-OHT) for 24 or 48 hours, unless the concentration was specified in the Figure legend. Stock solution of 20 mM 4-OHT dissolved in 96% ethanol was diluted to 100 μM prior treatment and was added to culture medium at ratio 1:100. Control *in vitro* cultures were incubated in the presence of 0.0048% ethanol (EtOH).

Immunofluorescence staining of intestinal organoids

Organoids were plated into 50% Matrigel droplet on glass-bottom 12-well plate and grown in complete organoid 1× ENR medium or complete organoid media containing WNT3A conditioned medium. Organoids were washed with 1× PBS and fixed with 4% PFA in PBS for 45 min at room temperature and blocked with 0.3% Triton X-100 in 1× PBS supplemented with 5% normal goat serum. Primary and secondary antibody staining followed the protocol used for staining intestinal tissue described above.

To quantify EdU incorporation in 2D monolayers, 2D cultures were grown to confluency, scratched, and grown for additional 12 hours, followed by treatment with 10 μM EdU in PBS for 30 minutes and fixation by 4% PFA. EdU was detected using Click-iT™ Plus EdU Cell Proliferation Kit for Imaging, Alexa Fluor™ 488 dye (ThermoFisher, C10637).

Flow cytometry

Freshly dissected small intestine was flushed with cold 1× PBS, opened lengthwise, and incubated at 37°C for 20 min in HBSS (Gibco, 14185-020) buffered with 10 mM HEPES (pH 8), and containing 10 mM DTT and 2% FBS, followed by 10 min wash in buffered HBSS containing 2% FBS. Next, intestine was cut into 0.5 mm pieces and incubated at 37°C for 20 min in buffered HBSS containing to 5 mM EDTA and 2% FBS, followed by vigorous shaking to mechanically release the epithelial cells. The suspension was filtered through a 40 μm cell strainer and cells were pelleted by centrifugation at 350 × g for 5 min. The resulting cell pellet was resuspended in buffered HBSS containing to 5 mM EDTA and 2% FBS and stained with antibodies for 30 min on ice. Prior sorting, DAPI was added, and DAPI and doublet exclusions were used in all cases. Cells were sorted using FACSAria II cell sorter (BD Bioscience) cell sorter and data were analyzed using FlowJo (Tree Star). For qPCR analysis intestinal stem cells or organoids were collected into 350 μL RLT buffer (Qiagen, 79216), for RNA sequencing, intestinal stem cells were collected into 500 μL sterile 1× PBS.

Quantitative PCR

Total RNA from 5,000 – 20,000 sorted intestinal cells or organoids were extracted using RNeasy Mini Kit (Qiagen, 74104) according to the manufacturer's protocol. cDNA was synthesized with High-capacity cDNA Reverse Transcription Kit (Applied Biosystems, 4368814). qPCR reactions were performed using iTaq Universal SYBR Green Supermix (Bio Rad, 1725121) in 384-well plates on a QuantStudio 6 Flex Real-Time PCR System (Thermo Fisher Scientific). Primers were purchased from Integrated DNA Technologies (IDT). Primer sequences and corresponding IDT identifiers are listed in Table S1.

RNA sequencing

In total, 5,000 – 10,000 ISCs were FACS sorted into 500 μl sterile PBS, pelleted and mRNA was isolated using the polyA Dynabeads mRNA direct Kit (Invitrogen, 61012) according to the manufacture's protocol. cDNA and libraries were made by the UCSF Genomic Core Laboratories using the SmartSeq/NexteraXT DNA library preparation Kits (Takarabio, 634471; Illumina, FC-131-1024). Three to five biological replicates were used for each condition. 50 bp single end sequencing was carried out on an Illumina HiSeq 4000. Sequencing reads were aligned to the Mouse reference genome (GRCm38.87) and the Ensembl gene annotation using STAR 2.4.2a.[121] Analysis for differential expression across the replicates was performed using DESeq2 v1.16.1.[122] Gene expression data was filtered based on outlier detection, low counts, and no counts per gene. Genes passing a multiple testing correction with p-value of 0.05 (FDR method) were considered significant.

CDC42 and RAC1 G-LISA activation assay

Intracellular levels of active CDC42 and RAC1 were measured using the G-LISA activation assay kit (Cytoskeleton, BK127 and BK128) according to manufacturer's guidelines. Briefly, intestinal organoids were FACS sorted into PBS, spun down, lysed in ice-cold lysis buffer provided by in the kit and snap frozen. Protein concentration was quantified, and additional lysis buffer was added to each sample to achieve equal protein concentration. Lysates were immediately used for colorimetric G-LISA assays according to the manufacturer's protocol.

Image acquisition and analysis

Fluorescence and bright-field images were acquired using a Leica inverted DMi8 microscope or Life Technology EVOS tissue culture microscope. Organoid 3D rendered z-stack images were acquired using a Leica inverted DMi8 microscope. Whole mount intestines were imaged using a Zeiss LSM 900 with Airyscan 2 confocal system. Live imaged organoids and stained organoids were acquired with a Zeiss Cell Observer spinning disc confocal system with incubation chamber. Images were processed with the open-source platform Fiji.[128] Quantifications of immunofluorescence stainings were performed manually using Fiji on the indicated number of villi, crypts, or fields of view per mice. Crypt bottom areas were segmented using the Weka segmentation tool in Fiji. Finally, the segmented crypt bottom areas were measured using the "Analyze Particles" function in Fiji.

QUANTIFICATION AND STATISTICAL ANALYSIS

Statistical significance between groups was determined using GraphPad Prism 9 (GraphPad Software, La Jolla, CA). The value N represents the number of animals or independent organoid preparations. Normally distributed data were analyzed using parametric Student's t-test with Welch's correction or one-way ANOVA with Tukey's multiple comparisons test. The non-parametric Mann–Whitney U-test was used if the data did not fit a normal distribution. Significance was taken as $P < 0.05$ with a confidence interval of 95%. Data are presented as mean ± SD for parametric data or as median ± interquartile range for non-parametric data.